Acta Pharmaceutica Sinica B 2026;16(8):5383−5404

Chinese Pharmaceutical Association
Institute of Materia Medica, Chinese Academy of Medical Sciences

Acta Pharmaceutica Sinica B

www.elsevier.com/locate/apsb
www.sciencedirect.com

ORIGINAL ARTICLE

Optimizing pyrazine-2-carboxamide derivatives as dual FLT3/HDAC inhibitors with enhanced pharmacokinetics and immunotherapeutic potential

Yingjie Chang[a,†], Xue Li[a,†], Huirui Wang[a,†], Huajun Zhao[c,†], Yue Zhou[b], Wenchao Bi[c], Ruixue Cheng[a], Yuxin Shi[a], He Weng[c], Xinying Yang[a], Wei Zhao[b,*], Hao Fang[a,*], Xuben Hou[a,*]

[a]*Department of Medicinal Chemistry, State Key Laboratory of Discovery and Utilization of Functional Components in Traditional Chinese Medicine, Shandong Key Laboratory of Druggability Optimization and Evaluation for Lead Compounds, Shandong Basic Science Special Academic Zone (Pharmacy), School of Pharmaceutical Sciences, Cheelo College of Medicine, Shandong University, Jinan 250012, China*
[b]*Department of Clinical Pharmacy, Institute of Clinical Pharmacology, Key Laboratory of Chemical Biology (Ministry of Education), NMPA Key Laboratory for Clinical Research and Evaluation of Innovative Drug, School of Pharmaceutical Sciences, Cheeloo College of Medicine, Shandong University, Jinan 250012, China*
[c]*Institute of Immunopharmaceutical Sciences, School of Pharmaceutical Sciences, Cheeloo College of Medicine, Shandong University, Jinan 250012, China*

Received 16 June 2025; received in revised form 15 April 2026; accepted 24 April 2026

KEY WORDS

HDAC;
FLT3;
Inhibitor;
Cancer immunotherapy

Abstract Dual FLT3/HDAC inhibition represents a promising synergistic strategy to address tumor heterogeneity. Building upon our prior lead **25h**, we developed novel 6-ethylpyrazine-2-carboxamide derivatives *via* systematic structural optimization to enhance pharmacokinetic properties and target selectivity. The optimized compound, CF-2-17, demonstrated potent dual inhibition of FLT3 (IC_{50} = 1.1 nmol/L) and HDACs (IC_{50} = 9.6 nmol/L), and exhibited a 27-fold selectivity for HDAC1 over HDAC6. Its improved physicochemical properties, including enhanced solubility and metabolic stability, translated into favorable plasma exposure *in vivo*. In the MOLM-13 (FLT3-ITD) xenograft model, oral administration of CF-2-17 showed antitumor efficacy comparable to combination therapy, without observable toxicity. CF-2-17 also exhibited antiproliferative activity against non-FLT3-ITD

*Corresponding authors.
E-mail addresses: zhao4wei2@hotmail.com (Wei Zhao), haofangcn@sdu.edu.cn (Hao Fang), hxb@sdu.edu.cn (Xuben Hou).
[†]These authors made equal contributions to this work.

Peer review under the responsibility of Chinese Pharmaceutical Association and Institute of Materia Medica, Chinese Academy of Medical Sciences.

https://doi.org/10.1016/j.apsb.2026.05.025

hematological malignancies and solid tumors, outperforming single-target agents. Furthermore, CF-2-17 effectively remodeled the tumor immune microenvironment through $CD4^+$ T cell activation and IFN-γ elevation, achieving 87% tumor growth inhibition in LLC syngeneic models. Mechanistically, CF-2-17 reversed FLT3 blockade-induced DC dysfunction *via* activation of the NF-κB pathway, thereby reinstating DC-mediated antitumor immunity. This dual FLT3/HDAC inhibitor demonstrates synergistic epigenetic-immune modulation, offering a promising approach for heterogeneous malignancies.

1. Introduction

Histone deacetylases (HDACs) are key epigenetic regulators in cancer, with inhibitors clinically effective against hematological malignancies[1-4]. The human HDAC family comprises 11 zinc-dependent isoforms divided into classes I (HDAC1-3, 8), IIa/b, and IV, alongside NAD^+-dependent sirtuins (Class III). Among these, Class I HDACs (particularly HDAC1/2) are frequently overexpressed in cancers and regulate oncogenic programs through chromatin remodeling and post-translational modification of non-histone proteins (*e.g.*, p53, STAT3)[5,6]. Although pan-HDAC inhibitors are effective in T-cell lymphomas and multiple myeloma[7], off-target toxicity and compensatory resistance pathways limit their clinical utility[8,9]. Recent structural biology advances enable the design of isoform-selective HDAC inhibitors and rational multi-target agents that synergize with other therapies to overcome tumor plasticity[10,11]. Notably, HDAC-based dual inhibitors show enhanced efficacy in solid tumors by simultaneously targeting oncogenic signaling and epigenetic reprogramming of the tumor microenvironment (Fig. 1A)[12-16].

Combining HDAC and FMS-like tyrosine kinase 3 (FLT3) inhibition is particularly promising for acute myeloid leukemia (AML)[17], where FLT3 mutations drive aggressive disease phenotypes[18,19]. FLT3, a receptor tyrosine kinase critical for hematopoietic stem cell survival, is mutated in ∼30% of AML cases, primarily *via* internal tandem duplications (FLT3-ITD) that confer constitutive activation[20-22]. First-generation FLT3 inhibitors (Midostaurin, Gilteritinib) combined with chemotherapy improve response rates in FLT3-mutated AML, but resistance inevitably arises from secondary FLT3 mutations or activation of parallel pathways (*e.g.*, RAS/MAPK, PI3K/AKT). Moreover, FLT3 inhibition alone fails to eradicate leukemia stem cells due to epigenetic plasticity, underscoring the need for combination therapy[23,24].

We previously showed the benefits of dual FLT3/HDAC inhibition using Gilteritinib and vorinostat (SAHA), which synergistically suppressed $FLT3\text{-}ITD^+$ AML proliferation *versus* monotherapies. This synergy led us to develop **25h**, an FLT3/HDAC dual inhibitor combining a Gilteritinib-derived hinge-binding motif with a zinc-binding group (Fig. 1B)[25]. Although **25h** showed potent enzymatic inhibition and anti-proliferative activity, poor physicochemical properties (*e.g.*, solubility below 1 μg/mL) and low HDAC isoform selectivity hindered its clinical translation. To address these limitations, we systematically optimized **25h**, by introducing hydrophilic groups into the linker bridging the pharmacophore of FLT3 and HDAC inhibitors (Fig. 1C). In particular, compound CF-2-17 retained nanomolar FLT3/HDAC1 inhibition (IC_{50} = 1.1/9.6 nmol/L), achieved 27-fold HDAC1/HDAC6 selectivity over **25h**, and exhibited significantly improved solubility. Interestingly, compound CF-2-17 reverses FLT3 inhibitor-induced dendritic cell dysfunction through epigenetic reprogramming, thereby expanding its therapeutic potential to solid tumors *via* tumor cell targeting and immune microenvironment remodeling.

2. Results and discussion

2.1. Structure−activity relationship of target compounds

In our previous study, we simplified the piperidin-4-ylpiperazine side chain of Gilteritinib to a piperazine moiety, a modification crucial for developing effective HDAC-FLT3 dual-target inhibitors, and thus retained this core feature in the current series. The dual inhibitory activities of the synthesized compounds against HDACs and FLT3 were first evaluated *via* enzymatic assays (Table 1).

Initial exploration with *N*-hydroxycinnamide derivatives featuring simple amide linkers (CF-2-1 to CF-2-3) yielded moderate HDAC inhibition (IC_{50} = 241.5−513.0 nmol/L against HeLa nuclear extracts), though less potent than vorinostat (SAHA, IC_{50} = 151.3 nmol/L). In contrast, their FLT3 inhibitory potency increased with linker length, culminating in CF-2-3 (IC_{50} = 0.5 nmol/L), which surpassed Gilteritinib (IC_{50} = 1.5 nmol/L). However, its cellular anti-proliferative activity was notably weaker (IC_{50} = 61 nmol/L), suggesting that an imbalanced dual-target profile may limit intracellular efficacy.

We next investigated ether-containing linkers (CF-2-4 to CF-2-8). While CF-2-4 to CF-2-6 maintained FLT3 inhibition comparable to Gilteritinib, only CF-2-6 retained HDAC inhibitory activity on par with SAHA (IC_{50} = 182.9 nmol/L). Consistent with its balanced enzymatic profile, CF-2-6 exhibited potent anti-proliferative activity (IC_{50} = 12.9 nmol/L), validating the dual-target strategy. Further elongation of the linker (CF-2-7, CF-2-8) diminished both HDAC inhibition and cellular potency without significantly affecting FLT3 binding, indicating that excessive linker flexibility may compromise the conformational restraint needed for optimal dual-target engagement in cells.

To modulate physicochemical properties and explore new chemical space, we introduced a tertiary amine into the linker, yielding compounds CF-2-10 to CF-2-19. Derivatives bearing *N*-hydroxyalkylamide or *N*-hydroxybenzamide as the zinc-binding group (ZBG) (CF-2-10 to CF-2-14) showed negligible HDAC inhibition at the highest concentration tested, despite retaining strong FLT3 inhibition (IC_{50} = 0.9−3.1 nmol/L). This highlights the critical influence of the ZBG on HDAC potency. In contrast, incorporation of the *N*-hydroxycinnamide ZBG in CF-2-15 restored potent dual inhibition, with IC_{50} values of 122.7 nmol/L (HDACs) and 2.0 nmol/L (FLT3). However, its cellular activity (IC_{50} = 19.7 nmol/L) was slightly inferior to Gilteritinib, suggesting potential limitations in cell permeability or intracellular distribution.

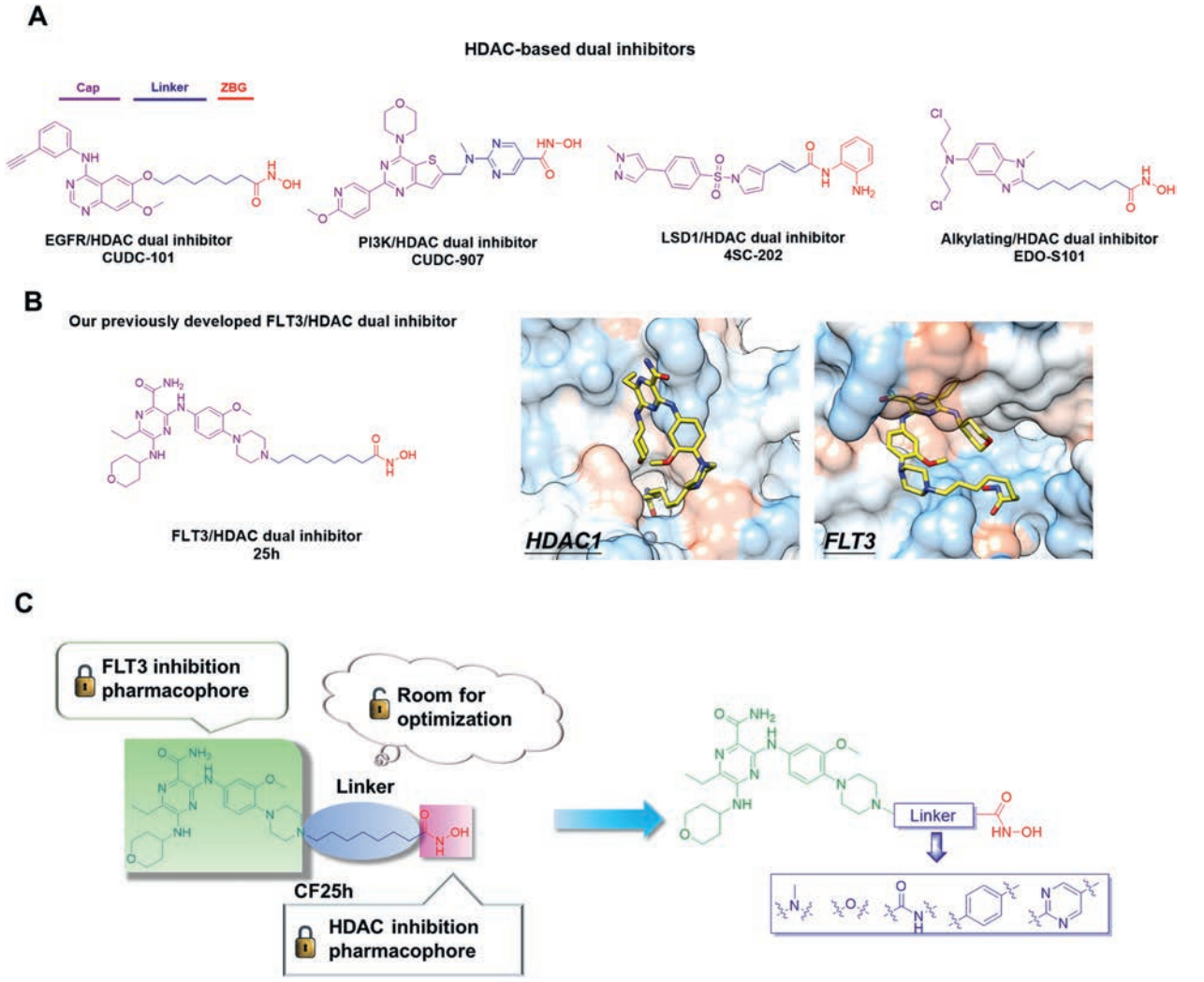

Figure 1 Rational design of novel FLT3/HDAC dual inhibitors. (A) Representative HDAC-based dual inhibitors. (B) Chemical structure of our previously developed FLT3/HDAC dual inhibitor **25h**. (C) Structure optimization strategy applied to design the new derivatives.

Notably, the *N*-hydroxypyrimidine-2-carboxamide derivatives (CF-2-16 to CF-2-19) consistently exhibited robust dual-target inhibition. Among these, CF-2-16 demonstrated moderate HDAC inhibition (IC_{50} = 180.9 nmol/L). Strikingly, further optimization led to CF-2-17, CF-2-18, and CF-2-19, which showed markedly enhanced HDAC inhibitory potency (IC_{50} = 43.3−56.8 nmol/L), surpassing SAHA. CF-2-17 was ultimately selected as the lead compound for advanced evaluation based on a superior overall profile: it delivered balanced and potent dual-target activity (IC_{50} (HDAC) = 43.3 nmol/L; IC_{50} (FLT3) = 1.1 nmol/L) coupled with good aqueous solubility (148.5 μg/mL at pH 7.0, Supporting Information Table S1). In contrast, the closely related analog CF-2-18 showed attenuated FLT3 inhibition (IC_{50} = 4.8 nmol/L), while CF-2-19, despite comparable potency, exhibited poor solubility (<1 μg/mL at pH 7.0, Table S1).

2.2. *Putative binding mode of CF-2-17*

To elucidate the structural basis for the potent dual-target activity of CF-2-17, molecular docking simulations were performed against FLT3 (PDB: 6JQR) and HDAC1 (PDB: 5ICN). The predicted binding modes corroborated our design rationale, demonstrating how the optimized molecular architecture engages key pharmacophoric elements of both targets. In the FLT3 kinase domain (Fig. 2A and C), the pyrazine-2-carboxamide core of CF-2-17 occupies the ATP-binding site. Key interactions include hydrogen bonds between the 2-carboxamide moiety and hinge residues Glu692 and Cys695, as well as an additional hydrogen bond from the secondary amine linker to Phe830. These contacts likely stabilize the inhibitor in a bioactive conformation, supporting its potent FLT3 inhibition. Simultaneously, CF-2-17 effectively engages the HDAC1 catalytic pocket (Fig. 2B and C). The *N*-hydroxypyrimidine-2-carboxamide group chelates the catalytic Zn^{2+} ion, while its hydroxamate oxygen hydrogen-bonds to the backbone of Gly149. The 2-carboxamide group also interacts with Tyr204 near the pocket entrance. This binding mode is characteristic of HDAC inhibitors and accounts for the observed enzymatic activity.

Collectively, these docking studies provide a coherent structural rationale for the balanced dual-inhibitory profile of CF-2-17. The molecular design successfully integrates distinct

Table 1 Inhibitory activities of target compounds against HDACs and FLT3, as well as antiproliferative activities against MOLM-13 cells.

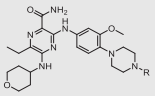

Compd.	R	IC_{50} (nmol/L) or inhibition rate		
		HDACs[a]	FLT3	MOLM-13
CF-2-1	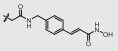	473.9 ± 25.0	1.4 ± 0.6	56.6 ± 13.5
CF-2-2	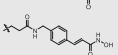	513.0 ± 131.7	1.5 ± 0.6	61.2 ± 35.3
CF-2-3	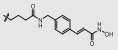	245.1 ± 144.5	0.5 ± 0.2	61.1 ± 9.3
CF-2-4	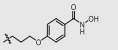	749.2 ± 184.3	1.0 ± 0.2	13.6 ± 3.0
CF-2-5	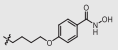	933.1 ± 203.8	1.8 ± 0.6	13.3 ± 3.4
CF-2-6	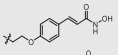	182.9 ± 24.2	2.0 ± 0.6	12.9 ± 1.2
CF-2-7	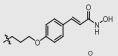	962.2 ± 331.4	1.0 ± 0.3	14.4 ± 1.4
CF-2-8	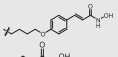	608.9 ± 100.7	3.5 ± 0.1	15.3 ± 5.6
CF-2-9	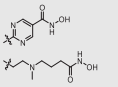	32.6 ± 12.1	1.8 ± 0.6	55.5 ± 28.0
CF-2-10	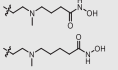	>10,000	3.1 ± 0.8	35.2 ± 6.5
CF-2-11	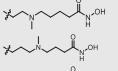	>10,000	0.9 ± 0.3	66.1 ± 8.4
CF-2-12	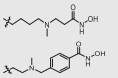	>10,000	1.2 ± 0.4	38.7 ± 5.6
CF-2-13	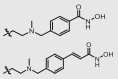	>10,000	1.0 ± 0.3	38.9 ± 12.5
CF-2-14		>10,000	2.0 ± 0.3	18.2 ± 3.0
CF-2-15	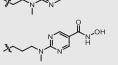	122.7 ± 7.8	2.0 ± 0.8	19.7 ± 3.3
CF-2-16	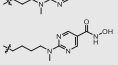	180.9 ± 10.5	2.5 ± 0.7	31.8 ± 4.4
CF-2-17	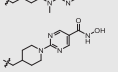	43.3 ± 1.2	1.1 ± 0.4	10.3 ± 2.9
CF-2-18	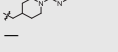	56.8 ± 9.4	4.8 ± 2.1	14.9 ± 0.6
CF-2-19	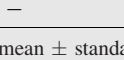	53.1 ± 5.1	1.2 ± 0.4	12.3 ± 3.6
SAHA	–	151.3 ± 24.0	N.D. [b]	471.3 ± 23.1
Gilteritinib	–	>10,000	1.5 ± 0.7	12.3 ± 0.4

[a]The values are expressed as mean ± standard deviation ($n = 3$).
[b]Not detected.

pharmacophores into a single entity capable of maintaining high-affinity interactions with both FLT3 and HDAC1, thereby validating our structure-based optimization strategy.

2.3. *Target selectivity profile of CF-2-17*

Based on its potent dual inhibition, we selected CF-2-17 for further study. It inhibited Class I HDACs more strongly than SAHA (Table 2). Specifically, CF-2-17 inhibited HDAC1 at nanomolar levels (IC_{50} = 9.6 nmol/L), 9-fold more potently than SAHA. It also potently inhibited HDAC2 (IC_{50} = 69.3 nmol/L) and HDAC8 (IC_{50} = 294.0 nmol/L), but weakly inhibited HDAC6 (IC_{50} = 259.6 nmol/L). These data indicate CF-2-17 has better Class I HDAC selectivity than lead compound **25h**. To elucidate the structural basis of this selectivity, we performed molecular dynamics (MD) simulations. The analysis revealed that CF-2-17 formed a more stable complex with HDAC1 than with HDAC6 (Supporting Information Fig. S1A). Notably, the FLT3-inhibitor fragment of CF-2-17 exhibited higher flexibility within the HDAC6 binding pocket (Fig. S1B), suggesting suboptimal complementarity that likely underlies the reduced inhibitory potency against this isoform. Interaction analysis corroborated this, showing that CF-2-17 forms a more complementary and consistent network of interactions within the HDAC1 active site (Fig. S1C).

To assess broader off-target potential, we profiled CF-2-17 against a panel of 20 kinases at a concentration of 10 nmol/L (Supporting Information Fig. S2). At this concentration, CF-2-17, exhibited potent inhibition of FLT3 and AXL, consistent with the characteristic target profile of its parent compound, Gilteritinib[26]. It also showed moderate activity against several additional kinases, most notably KIT, JAK2, and SRC, while maintaining little to no inhibition of kinases such as MET, FGFR1, HER2, and BRAF. This profile indicates that CF-2-17 shares a similar core kinase interaction pattern with Gilteritinib.

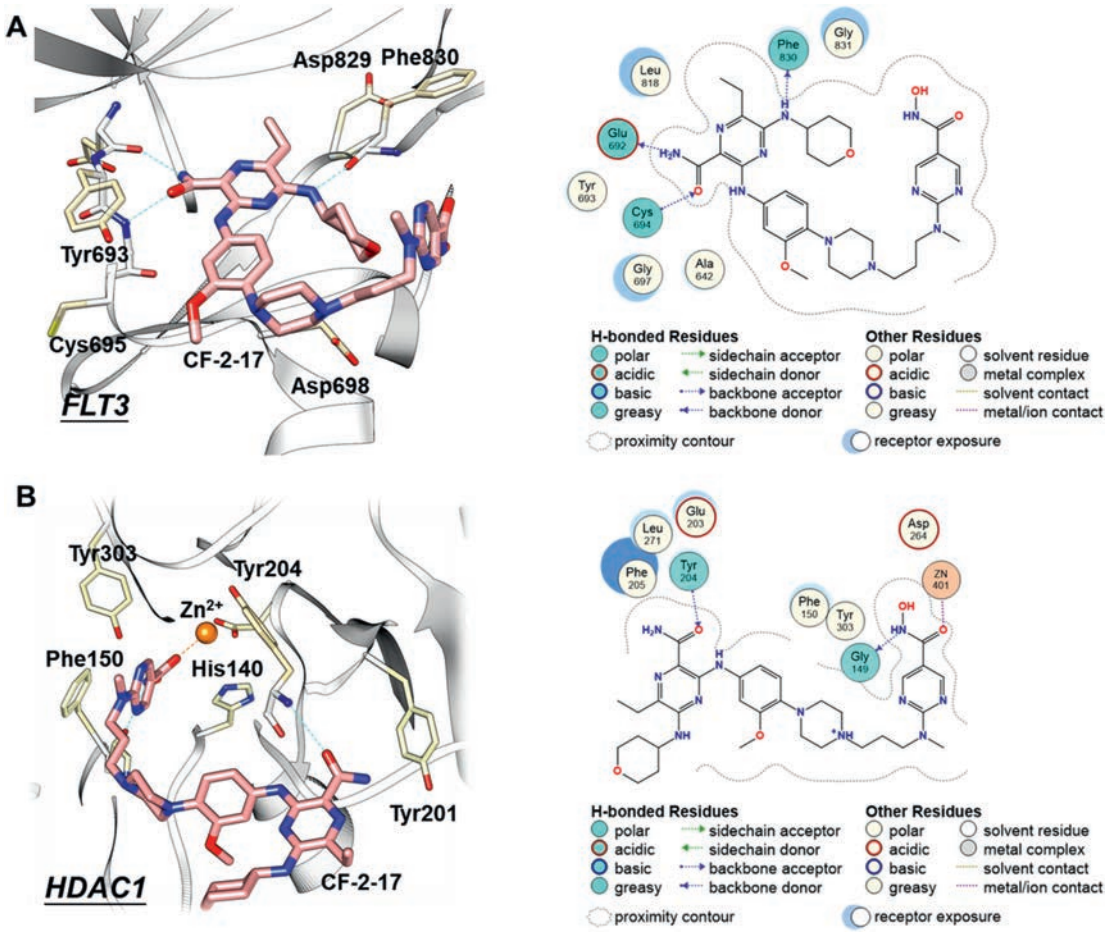

Figure 2 Predicted binding modes and interaction diagrams of CF-2-17 with FLT3 and HDAC1. (A) Predicted binding mode of compound CF-2-17 with FLT3 (PDB ID: 6JQR) and the corresponding two-dimensional ligand-interaction diagrams. (B) Predicted binding mode of compound CF-2-17 with HDAC1 (PDB ID: 5ICN) and the corresponding two-dimensional ligand-interaction diagrams.

2.4. Water solubility and metabolic stability of CF-2-17

We evaluated CF-2-17's water solubility, a key factor for distribution and metabolism. As shown in Table 3, its solubility in pH 2.0 and 7.0 PB buffers was 918.9 and 148.5 μg/mL, respectively, superior to **25h** and SAHA. This aligns with our design strategy and suggests improved pharmacokinetics.

CF-2-17 also showed enhanced metabolic stability. After 90 min incubation with mouse liver microsomes, CF-2-17 produced fewer metabolites than **25h**, indicating greater stability (Fig. 3A). In mouse plasma over 24 h, CF-2-17 remained largely intact, showing stability similar to **25h** (Fig. 3B). The *in vitro* metabolic stability data are summarized in Table 4. CF-2-17 exhibited a long half-life ($t_{1/2} \approx 283$ min, ~4.7 h) and a low intrinsic clearance ($CL_{int} = 0.00282$ mL/min/mg protein), indicative of high metabolic stability in liver microsomes. In contrast, the lead compound **25h** showed a shorter half-life ($t_{1/2} \approx 180$ min, ~3.0 h) and a higher clearance ($CL_{int} = 0.00416$ mL/min/mg protein). This direct comparison confirms that the structural optimization successfully improved the metabolic stability profile of CF-2-17.

Table 2 HDAC isoform selectivity of compounds CF-2-17.

Compd.	IC_{50} (nmol/L)[a]			
	HDAC1	HDAC2	HDAC6	HDAC8
CF-2-17	9.6 ± 3.2	69.3 ± 5.5	259.6 ± 11.9	294.0 ± 6.7
SAHA	89.3 ± 11.0	96.5 ± 22.3	23.8 ± 19.0	2430.7 ± 1028.5
25h[b]	18 ± 6	199 ± 76	8 ± 2	425 ± 41

[a]The values are expressed as mean ± standard deviation ($n = 3$).
[b]Data obtained from our previously study[25].

2.5. In vivo pharmacokinetic study of CF-2-17

We then evaluated the pharmacokinetics of CF-2-17 and **25h** *in vivo*. After intravenous administration at the same dose, CF-2-17 showed significantly higher plasma exposure

Table 3 Water solubility of compounds CF-2-17 and **25h.**

Compd.	Water solubility (μg/mL)[a]	
	PB (pH = 2.0)	PB (pH = 7.0)
CF-2-17	918.9 ± 178.6	148.5 ± 44.9
25h	212.2 ± 64.2	<1
SAHA	161.2 ± 19.3	115.5 ± 15.5

[a]The values are expressed as mean ± standard deviation ($n = 3$).

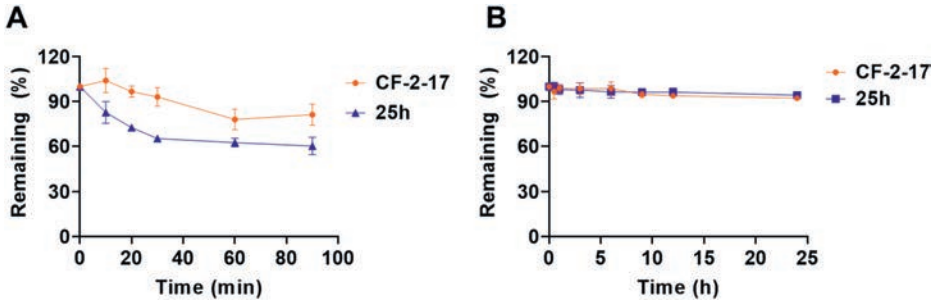

Figure 3 *In vitro* metabolic and plasma stability profiles of CF-2-17 and **25h.** (A) Remaining percentage of CF-2-17 and **25h** after incubation with mouse liver microsomes for the indicated times. (B) Remaining percentage of CF-2-17 and **25h** in mouse plasma over time. Data are expressed as mean ± SD from three independent biological replicates ($n = 3$).

Table 4 *In vitro* half-life and clearance of compounds CF-2-17 and **25h.**

Compd.	$t_{1/2}$ (min)[a]	$CL_{int,\ in\ vitro}$ (mL/min/mg protein)[a]
CF-2-17	283.0 ± 147.3	0.00282 ± 0.00114
25h	179.8 ± 66.8	0.00416 ± 0.00130

[a]The values were obtained from three independent experiments.

($AUC_{0-\infty}$ = 250.66 ng h/mL) than **25h** ($AUC_{0-\infty}$ = 9.15 ng h/mL) (Table 5). This superior exposure was also evident after oral dosing: plasma levels for CF-2-17 (C_{max} = 161 ng/mL, $AUC_{0-\infty}$ = 493.93 ng h/mL) far exceeded those for **25h** (C_{max} = 9.43 ng/mL, $AUC_{0-\infty}$ = 11.40 ng h/mL). Notably, CF-2-17 exhibited oral bioavailability (F = 19.71%), indicating favorable pharmacokinetic properties.

Notably, despite its high microsomal stability ($t_{1/2} \approx$ 4.7 h *in vitro*), CF-2-17 displayed a shorter *in vivo* plasma half-life (0.7 h). This discrepancy suggests that its systemic clearance is not primarily driven by hepatic CYP450 metabolism but may involve alternative pathways. To gain insight into its oral absorption, we performed computational profiling using *QikProp* module in Schrodinger Suite. The predictions indicate very low intestinal permeability (*e.g.*, Caco-2 $P_{app} < 25$ nm/s), aligned with its high polar surface area (~195 Å^2) and molecular weight (~664 Da). The predicted human oral absorption (15.85%) closely matches the experimental bioavailability, supporting the conclusion that permeability is a key limiting factor. This provides a rationale for the observed bioavailability and directs future optimization strategies toward improving absorption properties.

2.6. *Intracellular inhibition of FLT3 and HDAC by CF-2-17*

We assessed intracellular target engagement using key HDAC substrates. In MOLM-13 cells, CF-2-17 dose-dependently increased acetylated histone H3 levels more effectively than SAHA. Unlike the pan-inhibitor SAHA, CF-2-17 only weakly increased acetylated α-tubulin (an HDAC6 substrate), with a significant effect only at high concentrations (Fig. 4A). This aligns with its HDAC isoform selectivity profile (Table 2). In addition, we explored other histone modifications by examining the effect of CF-2-17 on histone H3 lysine 4 trimethylation (H3K4me3), a canonical mark of active transcription. As shown in Supporting Information Fig. S3, CF-2-17 treatment significantly increased global H3K4me3 levels. This finding provides direct evidence that CF-2-17's epigenetic impact is pleiotropic. CF-2-17 also potently inhibited FLT3 signaling pathways. As shown in Fig. 4B and C, CF-2-17 dose-dependently suppressed phosphorylation of FLT3, STAT5, and ERK1/2 in MOLM-13 cells, outperforming Gilteritinib, particularly for p-ERK. This confirms CF-2-17's dual targeting mechanism. Consistent with our prior findings on **25h**[25], dual FLT3/HDAC inhibition provides unique pathway modulation. CF-2-17 (6 h treatment) reduced p-ERK levels in MOLM-13 cells more effectively than single agents or their combination (Fig. 4D), demonstrating its superiority in blocking key survival signals.

2.7. *Impacts of CF-2-17 on cell apoptosis and cell cycle*

Using Annexin V-FITC/PI staining, we found CF-2-17 induced apoptosis in MOLM-13 cells most effectively after 24 h treatment among tested compounds (Fig. 5A). At 0.1 μmol/L, CF-2-17 induced ~70% apoptosis, exceeding Gilteritinib, SAHA, or their combination (Fig. 5B). CF-2-17 also induced mitochondrial membrane potential loss, an early apoptosis marker, in a

Table 5 Pharmacokinetic parameters of compounds CF-2-17 and 25h.

Parameters	CF-2-17[a]		25h[a]	
	i.v. (1 mg/kg)	*p.o.* (10 mg/kg)	i.v. (1 mg/kg)	*p.o.* (10 mg/kg)
$t_{1/2}$ (h)	0.70	0.93	1.09	0.865
T_{max} (h)	0.08	2.01	0.0833	0.333
C_{max} (ng/mL)	431.12	161.24	6.62	9.43
AUC_{0-t} (ng/mL·h)	241.69	490.85	7.34	8.89
$AUC_{0-\infty}$ (ng/mL·h)	250.66	493.93	9.15	11.4
F (%)		19.71		24.9

[a]The values were obtained from three independent experiments.

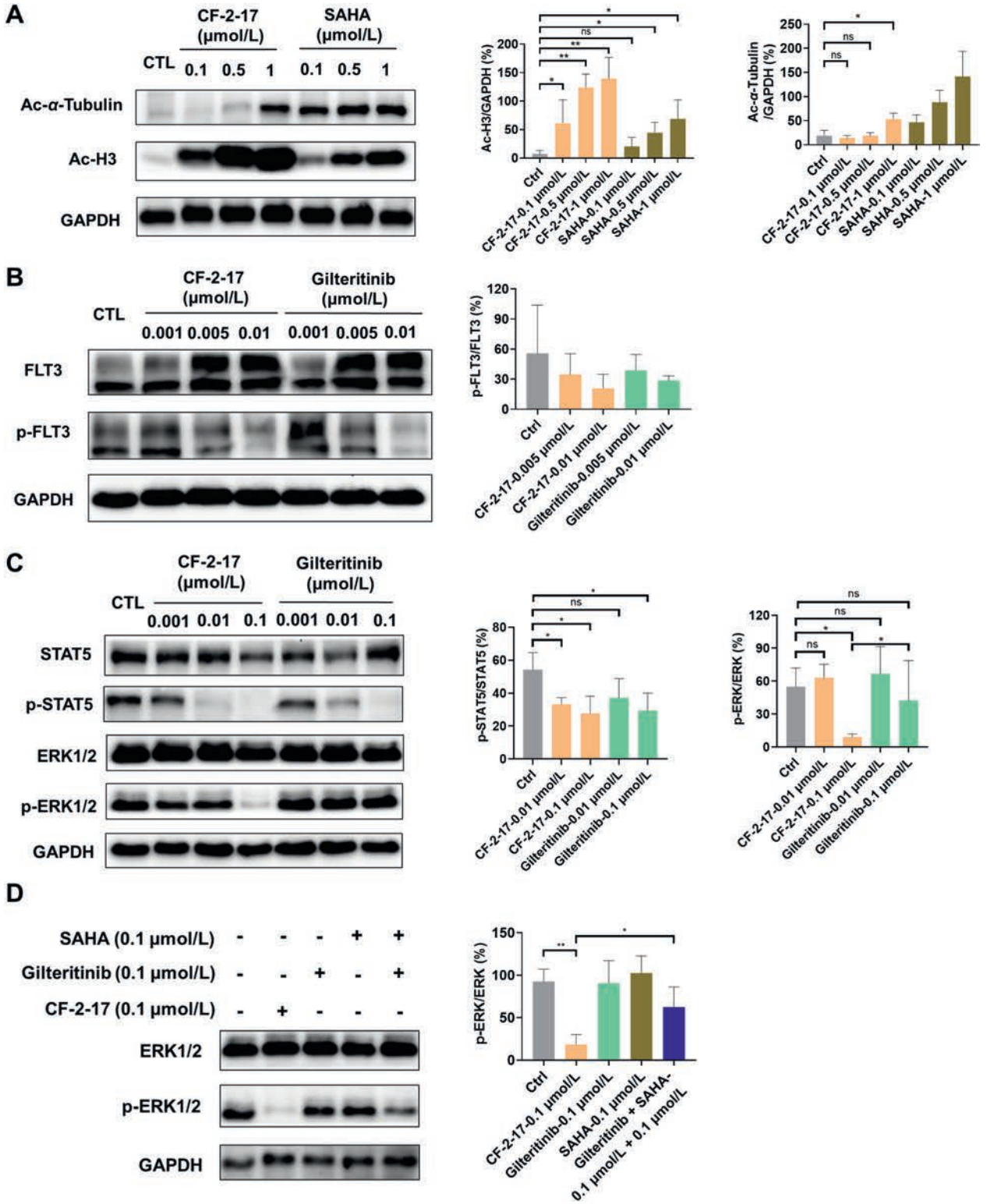

Figure 4 CF-2-17 modulates dual-target biomarkers and downstream signaling pathways in MOLM-13 cells. (A) Levels of acetylated α-tubulin (Ac-α-Tub) and acetylated histone H3 (Ac-H3) after 6 h treatment. (B) Levels of phosphorylated FLT3 (p-FLT3) after 6 h treatment. (C) Levels of phosphorylated STAT5 (p-STAT5) and ERK (p-ERK) after 6 h treatment. (D) Sustained suppression of p-ERK by CF-2-17 compared to Gilteritinib, SAHA, and their combination over a 24-h time course. Data are expressed as mean ± SD from three independent biological replicates ($n = 3$). Statistical analysis was carried out between the data of each group (ns meaning no significant difference, $^{*}P < 0.05$, and $^{**}P < 0.01$).

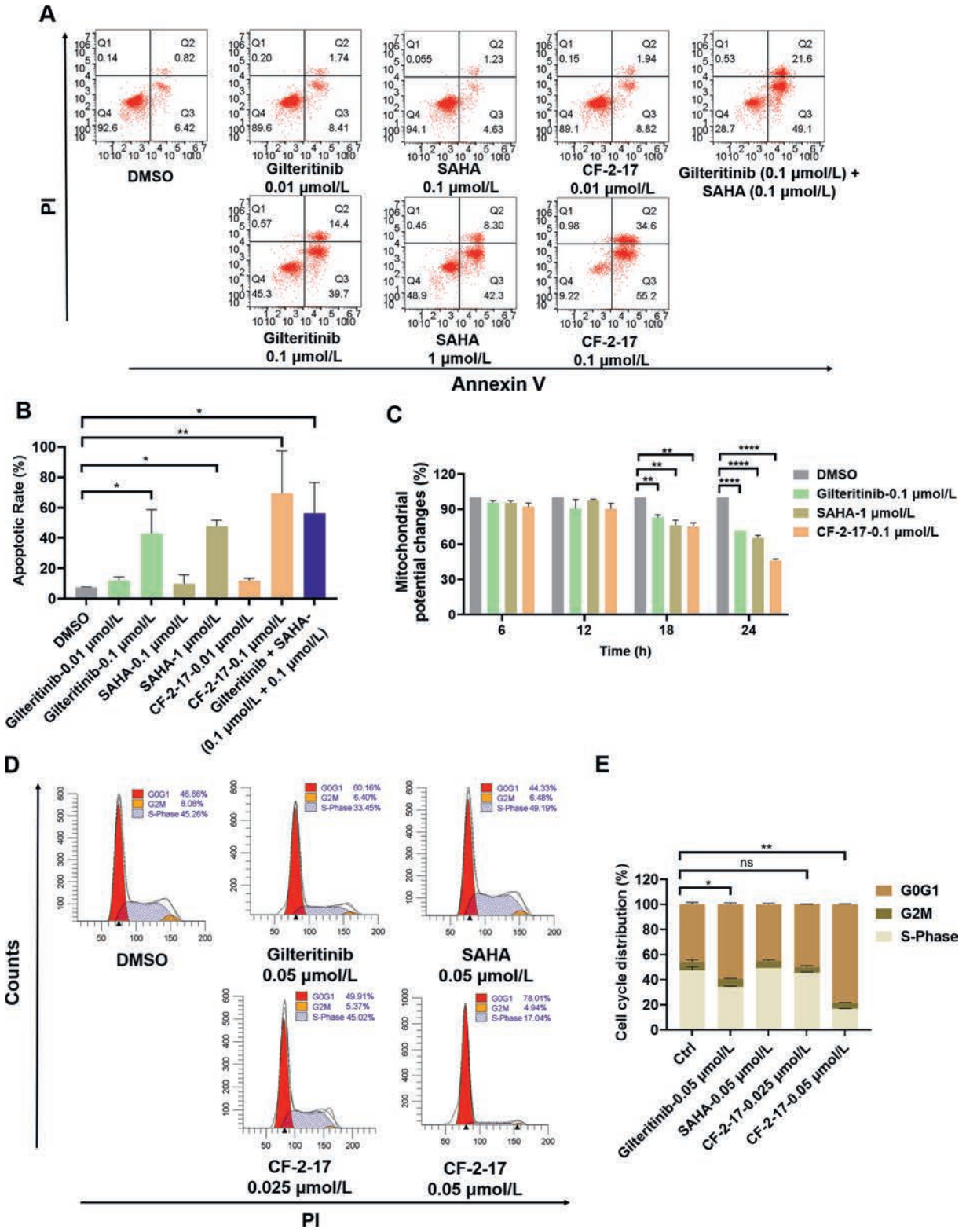

Figure 5 CF-2-17 induces apoptosis, mitochondrial dysfunction, and cell cycle arrest in MOLM-13 cells. (A, B) Apoptosis induction assessed by Annexin V/PI staining after treatment with CF-2-17, Gilteritinib, or SAHA. (C) Reduction in mitochondrial membrane potential ($\Delta\Psi_m$) detected by JC-1 staining. (D, E) Cell cycle distribution analyzed by PI staining. Data are expressed as mean ± SD from three independent biological replicates ($n = 3$). Statistical analysis was carried out between the data of each group (ns meaning no significant difference, $^*P < 0.05$, $^{**}P < 0.01$, and $^{****}P < 0.0001$).

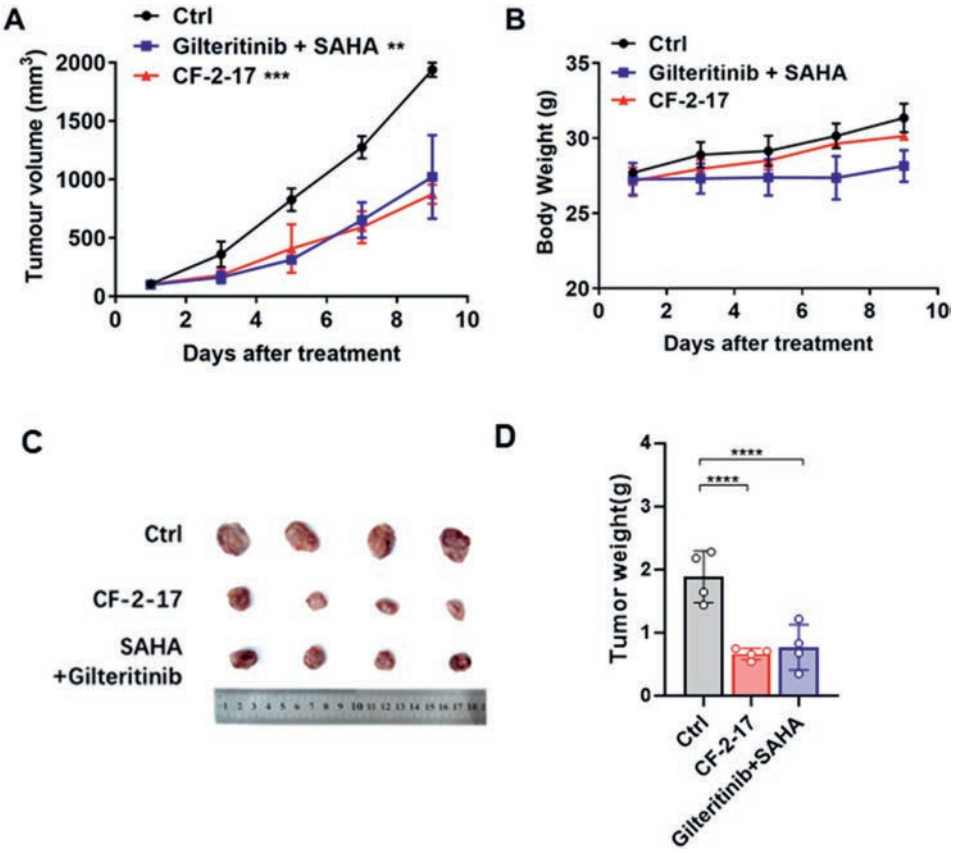

Figure 6 CF-2-17 exerts anti-tumor activity in a MOLM13 xenograft model. (A) Tumor volume changes of each group during treatment. (B) Body weight changes of each group during treatment. (C) Tumor images of each group after treatment. (D) Tumor weight of each group after treatment. Data are expressed as mean ± SD from four biologically independent mice ($n = 4$). Statistical analysis was carried out between the data of each group (**$P < 0.01$, ***$P < 0.001$, and ****$P < 0.0001$).

time-dependent manner more potently than Gilteritinib or SAHA (Fig. 5C), consistent with its strong pro-apoptotic effect. Furthermore, CF-2-17 (24 h treatment) caused more significant G0/G1 phase arrest in MOLM-13 cells than Gilteritinib or SAHA, as shown by flow cytometry (Fig. 5D and E).

2.8. In vivo anti-tumor efficacy in MOLM-13 xenograft tumor models

We compared the FLT3/HDAC dual inhibitor CF-2-17 to combination therapy in MOLM-13 xenografts. Mice bearing subcutaneous MOLM-13 tumors (~100 mm^3) received daily oral doses of vehicle, CF-2-17 (10 mg/kg), or Gilteritinib + SAHA (10 + 30 mg/kg). CF-2-17 suppressed tumor growth significantly *versus* vehicle and showed greater efficacy (TGI = 64.7%) than the combination (TGI = 59.2%) (Fig. 6A–C and D). Mice receiving the combination lost weight, while CF-2-17-treated mice maintained stable weights, indicating lower toxicity (Fig. 6B). These results demonstrate CF-2-17's improved efficacy and safety profile in FLT3-ITD AML.

2.9. Anti-proliferation activity of CF-2-17 against non-FLT3-ITD tumors

Given the role of HDAC inhibitors in epigenetic reprogramming and tumor sensitization[27,28], we sought to evaluate the anti-proliferation activities of CF-2-17 against non-FLT3-ITD tumors. Similar with the result in MOLM-13 cells (IC_{50} = 0.012 μmol/L), CF-2-17 showed good anti-proliferation activity in MV-4-11 cells (FLT3-ITD) (Table 6). Interestingly, CF-2-17 showed potent anti-proliferative activity (IC_{50} = 0.66–0.73 μmol/L) in non-FLT3-ITD hematological tumor cells (THP-1, K562), exceeding Gilteritinib and SAHA (Table 6). It also showed efficacy in solid tumor cells (PC-9, Ovcar3, LLC, MC-38), with IC_{50} values (0.42–0.72 μmol/L) lower than Gilteritinib and SAHA. The contribution of dual FLT3/HDAC inhibition to non-FLT3-ITD cells was further supported by the synergistic effect observed for the combination treatment of

Table 6 The anti-proliferative activity of compound CF-2-17 against other tumor cells.

Tumor cells	IC_{50} (μmol/L)[a]		
	CF-2-17	Gilteritinib	SAHA
MV-4-11	0.012 ± 0.003	0.011 ± 0.003	0.60 ± 0.08
THP-1	0.66 ± 0.14	2.58 ± 0.40	1.66 ± 0.74
K562	0.73 ± 0.07	6.41 ± 1.59	1.11 ± 0.32
A549	3.70 ± 0.63	8.63 ± 4.07	5.62 ± 3.53
PC-9	0.63 ± 0.12	3.51 ± 0.93	0.86 ± 0.18
Ovcar3	0.72 ± 0.14	0.79 ± 0.10	2.63 ± 0.80
LLC	0.42 ± 0.10	1.06 ± 0.28	2.38 ± 1.04
MC-38	0.81 ± 0.24	2.73 ± 1.41	1.9 ± 0.29

[a]The values were obtained from three independent experiments.

Gilteritinib and SAHA (Supporting Information Fig. S4). Thus, CF-2-17 maintains sensitivity in FLT3-ITD AML while showing superior activity against non-FLT3-ITD hematological and solid tumors.

Given that FLT3-ITD mutations are often accompanied by secondary mutations such as F691L, leading to resistance to FLT3 inhibitors, we further evaluated the activity of CF-2-17 against this clinically relevant resistant mutant. As summarized in the Supporting Information Table S2, CF-2-17 was tested alongside Gilteritinib in isogenic Ba/F3 cell lines engineered to express either FLT3-ITD or FLT3-ITD-F691L. In the FLT3-ITD context, CF-2-17 showed comparable potency to Gilteritinib. Critically, in the FLT3-ITD-F691L setting, CF-2-17 (IC_{50} = 10.6 nmol/L) demonstrated an approximately 3-fold higher potency than Gilteritinib (IC_{50} = 33.2 nmol/L). This indicates that CF-2-17 retains better activity against this resistant mutation. While these data on the F691L mutant are promising, profiling against a full panel of clinically observed resistance mutations (*e.g.*, D835Y) remains an essential direction for future investigation.

Furthermore, we evaluated the therapeutic efficacy of CF-2-17 in non-FLT3-ITD hematologic malignancies. In an established K562 subcutaneous xenograft model (Fig. 7A), CF-2-17 significantly inhibited tumor progression, as evidenced by marked reductions in tumor volume and weight (Fig. 7B−D). Notably, CF-2-17 exhibited superior anti-tumor activity compared to the other inhibitors (Gilteritinib, SAHA, and the dual-target inhibitor CUDC-907). Subsequently, all treatment groups maintained stable body weights throughout the experimental period without significant decline, indicating that CF-2-17 possesses favorable tolerability while exerting effective anti-tumor activity (Fig. 7E).

2.10. RNA-seq analysis in MOLM-13 cells treated with CF-2-17

HDAC inhibitors are involved in the development and progression of tumors primarily through regulating gene expression and transcription. To further elucidate the intrinsic antitumor mechanisms of CF-2-17, we conducted mRNA-level analysis in MOLM-13 cells treated with CF-2-17. Utilizing KEGG pathway enrichment analysis and Gene Ontology (GO) functional annotation, we aimed to clarify its regulatory effects on signaling pathways and biological processes.

As illustrated in Fig. 8A, CF-2-17 was capable of upregulating multiple tumor suppressor genes, including RNASET2 and PLD3, RNASET2 regulates tumor cell invasion and metastasis by suppressing cholesterol metabolism-mediated RTK family member stability and downstream ERK signaling pathway activation, while PLD3 regulates cell cycle and proliferation through the p53/ZEB1-PLD3 axis and DNA methylation mechanisms[29,30]. Concurrently, CF-2-17 also significantly enhanced the expression of multiple antitumor immune-related genes, including CD70, TYROBP, and CSF3R. Among these, CD70, as a key immune costimulatory molecule, can effectively enhance T cell-mediated antitumor immune responses[31], while TYROBP participates in the transduction of immune cell activation signals[32], associating with regulating immune synapse formation and cytotoxic functions.

Further KEGG enrichment analysis demonstrated that differentially expressed genes (DEGs) were implicated not only in tumor growth-associated pathways, such as cell cycle, cellular senescence, apoptosis, and energy metabolism, but also in the modulation of antigen processing and presentation (Fig. 8B).

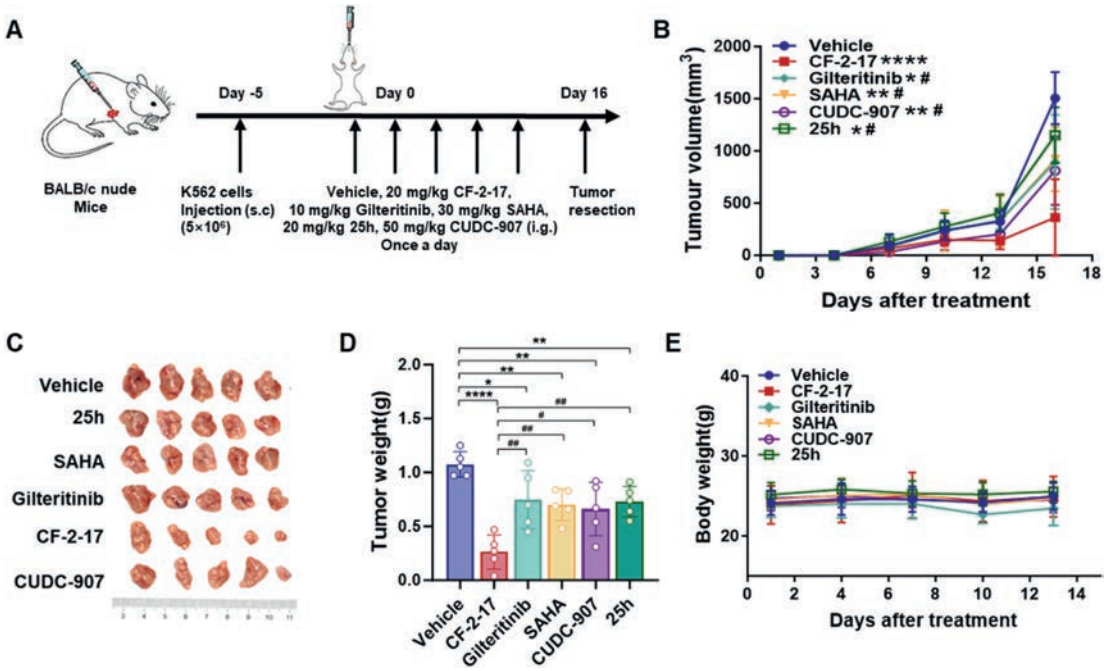

Figure 7 Antitumor efficacy of CF-2-17 in a K562 xenograft model. (A) K562 cells were transplanted into C57BL/6J mice and treatment with of vehicle (qd, i.g.), Gilteritinib (qd, i.g.), SAHA (qd, i.g.), **25h** (qd, i.g.), CUDC-907(qd, i.g.) and CF-2-17 (qd, i.g.). (B) Tumor growth curves showing mean tumor volume over time. (C) Tumor images of each group after treatment. (D) Final tumor weights measured at the endpoint of the study. (E) Changes in mean body weight of mice during the treatment period. Data are expressed as mean ± SD from five biologically independent mice (n = 5). Statistical analysis was carried out between the data of each group. *$P < 0.05$, **$P < 0.01$, and ****$P < 0.0001$ *versus* vehicle; $^{\#}P < 0.05$ and $^{\#\#}P < 0.01$ *versus* the CF-2-17 (20 mg/kg) group.

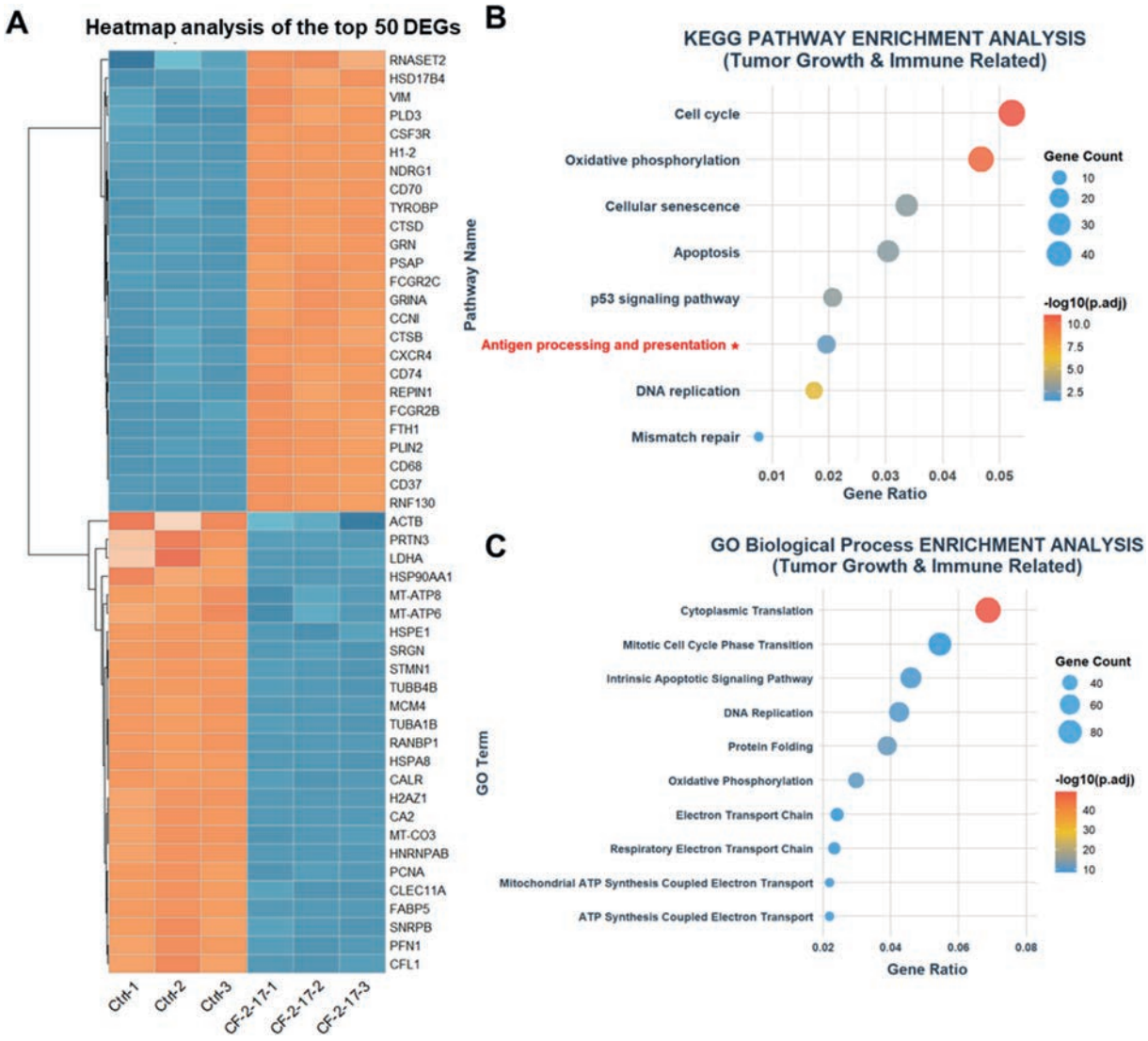

Figure 8 Transcriptomic profiling reveals CF-2-17 modulates multiple pathways in MOLM-13 cells. (A) Heatmap of the top 50 differentially expressed genes (DEGs). (B) Significantly enriched KEGG pathways of the DEGs. (C) Significantly enriched Gene Ontology (GO) terms in the biological process category. RNA-seq was performed using three independent biological replicates per group ($n = 3$).

Correspondingly, GO functional annotation revealed that CF-2-17 treatment engages biological processes that promote tumor immunogenicity, including DNA replication, translation, protein folding, and energy metabolism, while also facilitating apoptosis-mediated tumor cell elimination (Fig. 8C). Together, these results indicate that CF-2-17 may exert its therapeutic efficacy through the activation of antitumor immune responses.

2.11. Anti-tumor activity of CF-2-17 in the LLC allograft models

As shown in Fig. 9A, CF-2-17 inhibited LLC cell proliferation more potently ($IC_{50} = 0.42$ μmol/L) than Gilteritinib, SAHA, or their combination *in vitro*. In the LLC allograft model, oral CF-2-17 (16 days) significantly reduced tumor volume and weight *versus* vehicle without significant body weight loss (Fig. 9B−F). High-dose CF-2-17 showed superior anti-tumor activity (TGI = 87.5%) over Gilteritinib, SAHA, and the combination (Fig. 9D, Supporting Information Fig. S5). Organ weights confirmed minimal toxicity at experimental doses (Supporting Information Fig. S6). In addition, histopathological examination by H&E staining demonstrated that monotherapy with CF-2-17, Gilteritinib, or SAHA significantly alleviated pulmonary burden in LLC-bearing mice compared to the model control group (Supporting Information Fig. S7). Notably, while the Gilteritinib and SAHA combination group induced hemorrhagic renal toxicity, no such adverse effect was observed in the CF-2-17 monotherapy cohort.

Moreover, we conducted acute toxicity experiments in mice to further substantiate the safety of CF-2-17. First, during treatment with CF-2-17 at different concentrations, mice maintained a 100% survival rate (Supporting Information Fig. S8A). Second, CF-2-17 did not induce upregulation of ALT or AST, indicating no apparent liver damage (Fig. S8B). Complete blood counts revealed that treatment with various concentrations of CF-2-17 had no significant effect on the absolute numbers of any blood cell types

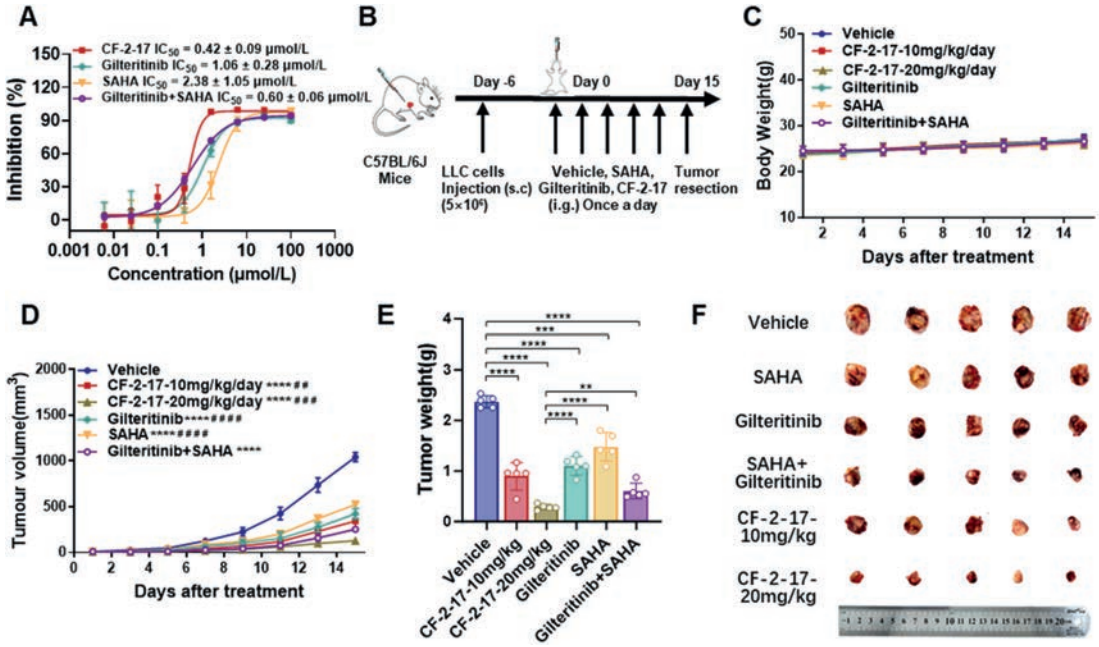

Figure 9 CF-2-17 demonstrates superior anti-tumor efficacy against LLC compared to Gilteritinib, SAHA, and their combination. (A) The anti-proliferative activity of CF-2-17, Gilteritinib and SAHA against LLC cells. (B) LLC cells were transplanted into C57BL/6J mice and treatment with of vehicle (qd, i.g.), SAHA (qd, i.g.), Gilteritinib (qd, i.g.), Gilteritinib + SAHA (qd, i.g.) and CF-2-17 (qd, i.g.). (C) Body weight changes of each group during treatment. (D) Tumor volume changes of each group during treatment. (E) Tumor weights of each group after treatment. (F) Tumor images of each group after treatment. Data are expressed as mean ± SD from five biologically independent mice ($n = 5$). Statistical analysis was carried out between the data of each group (**$P < 0.01$, ***$P < 0.001$ and ****$P < 0.0001$ *versus* vehicle; $^{\#\#}P < 0.01$, $^{\#\#\#}P < 0.001$ and $^{\#\#\#\#}P < 0.0001$ *versus* Gilteritinib + SAHA).

compared to the vehicle group (Fig. S8C). Additionally, CF-2-17 treatment group showed no significant changes in body weight (Fig. S8D).

Furthermore, the hERG assay yielded an IC_{50} value of >30 μmol/L for CF-2-17 (Supporting Information Fig. S9). This concentration represents a margin of >2500-fold over its cellular anti-proliferative IC_{50} in MV-4-11 cells (0.012 ± 0.003 μmol/L, Table 6) and >123-fold over its peak plasma concentration (C_{max}) following oral administration (161.24 ng/mL, Table 5) at efficacious doses, indicating a very low risk of relevant hERG channel inhibition.

2.12. *CF-2-17 stimulate anti-tumor immunity*

To investigate the immunomodulatory effects of CF-2-17 in the tumor microenvironment, we analyzed tumor-infiltrating lymphocytes from the LLC allograft model (Fig. 9B). T cell-mediated immune responses are critical in antitumor immunity. Compared with the vehicle group, treatments with CF-2-17, Gilteritinib, SAHA, and their combination significantly increased the tumor-infiltrating of T cells (Fig. 10A–C). Notably, CF-2-17 and the combination group reduced the proportions of $Tim3^+$ exhausted $CD4^+$ and $CD8^+$ T cells, which was conducive to T cell-mediated immune responses (Fig. 10D). Furthermore, all treatments significantly enhanced the production of effector molecules IFN-γ and TNF-α in both $CD4^+$ T cells (Fig. 10E and F) and $CD8^+$ T cells (Fig. 10G and H), while CF-2-17 and SAHA demonstrated greater enhancement compared to Gilteritinib. These findings indicate that CF-2-17 synergistically remodels the immune microenvironment through dual mechanisms: suppressing Tim3-mediated T cell exhaustion and amplifying IFN-γ/TNF-α effector functions.

Given the critical role of immune checkpoints in regulating antitumor immunity, we further assessed the expression of programmed death-ligand 1 (PD-L1) in tumor tissues. While SAHA treatment upregulated PD-L1, consistent with reports for some HDAC inhibitors[33,34], both Gilteritinib and CF-2-17 significantly suppressed PD-L1 expression compared to the vehicle group (Supporting Information Fig. S10). This result indicates that CF-2-17, unlike SAHA, does not induce this potential adaptive immune resistance mechanism and may contribute to sustaining an immunostimulatory microenvironment.

2.13. *CF-2-17 enhances dendritic cell function*

We next evaluated the impact of CF-2-17 on dendritic cells (DCs) using tumor and spleen samples from the aforementioned LLC tumor-bearing mice (Fig. 9B). Previous study has indicated the FLT3 inhibition may disrupt the function of FLT3-FLT3L axis in dendritic cells (DCs), which play a critical role in initiating adaptive immunity. To elucidate the mechanisms underlying the activation of anti-tumor immunity by CF-2-17, we further investigated the tumor infiltering DCs and spleen DCs.

Specifically, conventional type 1 dendritic cells (cDC1) primarily activate $CD8^+$ T cell-mediated cytotoxic immunity through cross-presentation pathways, while conventional type 2 dendritic cells (cDC2) initiate $CD4^+$ T cell helper immunity *via* MHC class II-dependent antigen presentation. Compared with the vehicle group, FLT3 inhibitor Gilteritinib showed no significant differences in DC proportions or function. In contrast, CF-2-17, SAHA,

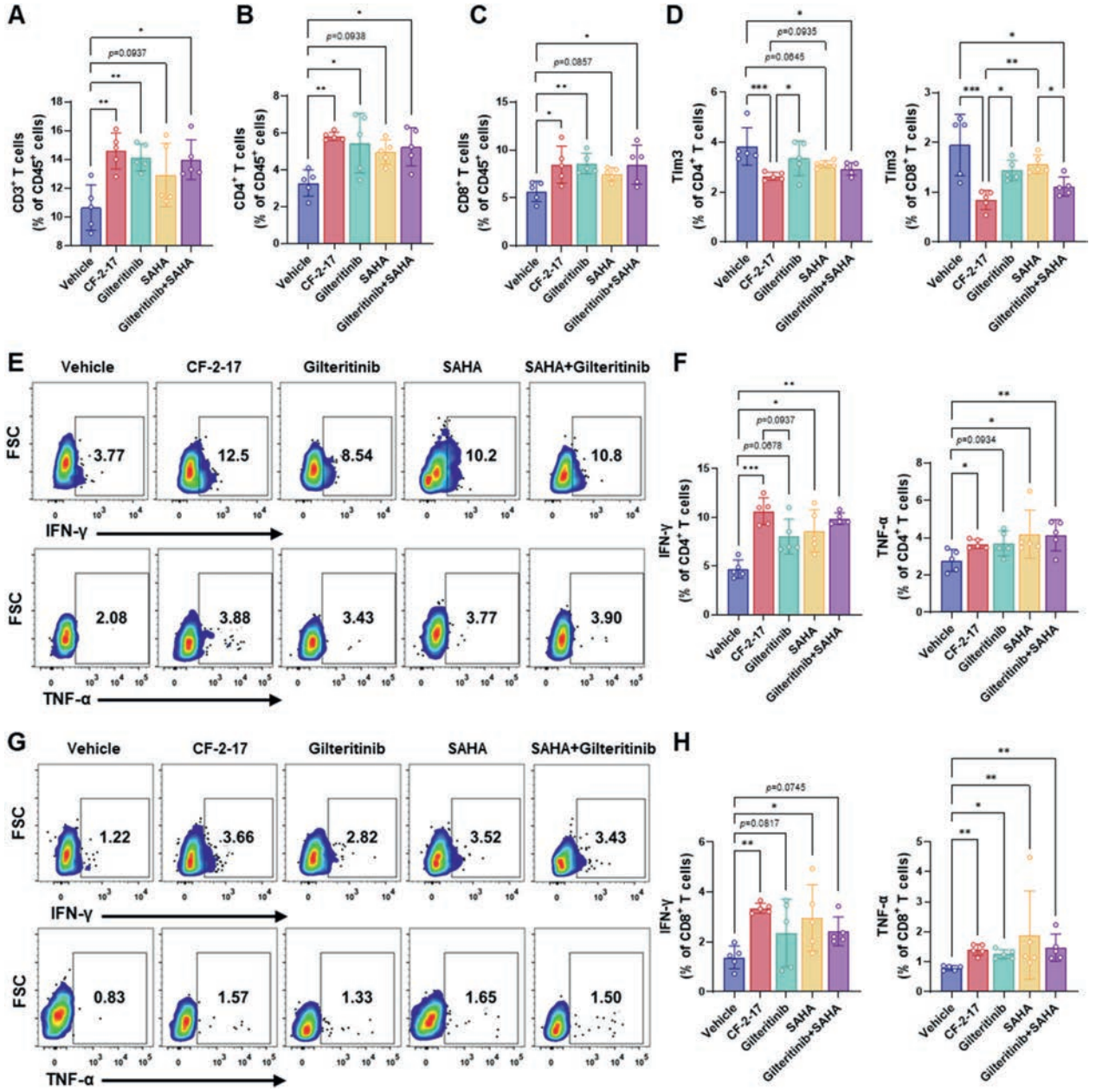

Figure 10 *In vivo* analysis of T cell infiltration and function in LLC tumors. (A−C) The proportions of $CD3^+$ (A), $CD4^+$ (B), and $CD8^+$ T cells (C) in $CD45^+$ cells in tumors of each group. (D) The expression of Tim3 on $CD4^+$ and $CD8^+$ T cells in tumors of each group. (E−H) The expressions of IFN-γ and TNF-α on $CD4^+$ (E, F) and $CD8^+$ (G, H) T cells in tumors of each group. Data are expressed as mean ± SD from five biologically independent mice ($n = 5$). Statistical analysis was carried out between the data of each group (*$P < 0.05$, **$P < 0.01$ and ***$P < 0.001$).

and their combination group significantly increased DC infiltration and upregulated CD86 expression, indicating enhanced DC activation (Fig. 11A and B). Notably, while Gilteritinib reduced both proportion and function of cDC1, CF-2-17 and SAHA preserved cDC1 proportions while elevating CD86 expression (Fig. 11C and D). Regarding cDC2, CF-2-17 and SAHA markedly promoted cDC2 development and activation, whereas Gilteritinib exhibited no effect on cDC2 population (Fig. 11E and F). These findings indicated that CF-2-17 and SAHA enhance antitumor immunity by promoting DC accumulation and activation in tumor. In contrast, single-target FLT3 inhibition lacks these immunostimulatory effects and even impairs cDC1 function.

Similar phenomena were observed in the spleen DCs. CF-2-17, SAHA, and their combination significantly increased the proportions of DCs, cDC1, and cDC2 while enhancing CD86 expression to boost antigen-presenting capacity, whereas Gilteritinib groups showed no significant differences from the vehicle group (Fig. 12A−F). CD8α and CD103 serve as functional discriminators for cDC1 subsets: $CD8\alpha^+$ cDC1 primarily encounter antigens in lymphoid tissues, while $CD103^+$ cDC1 respond to peripheral antigenic signals. CF-2-17, SAHA, and the combination preferentially upregulated $CD8\alpha^+$ cDC1 proportions and function while exerting minimal effects on $CD103^+$ cDC1 (Fig. 12G−I). Conversely, Gilteritinib significantly reduced

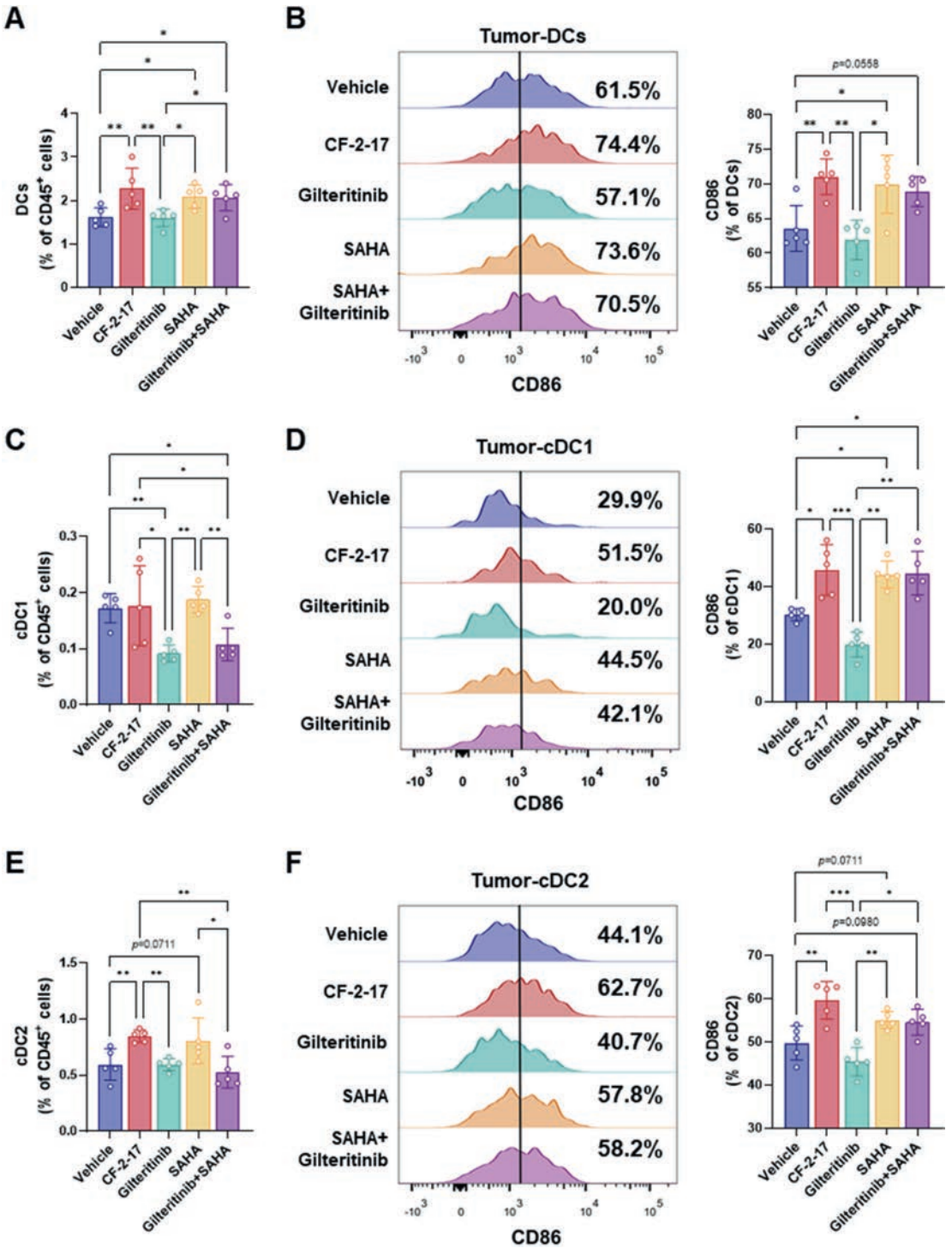

Figure 11 *In vivo* analysis of dendritic cell subsets and activation in LLC tumors. (A, C, E) The proportions of DCs (A), cDC1 (C), and cDC2 (E) in $CD45^+$ cells in tumors of each group. (B, D, F) The expression of CD86 on DCs (B), cDC1 (D), and cDC2 (F) in tumors of each group. Data are expressed as mean ± SD from five biologically independent mice ($n = 5$). Statistical analysis was carried out between the data of each group (*$P < 0.05$, **$P < 0.01$ and ***$P < 0.001$).

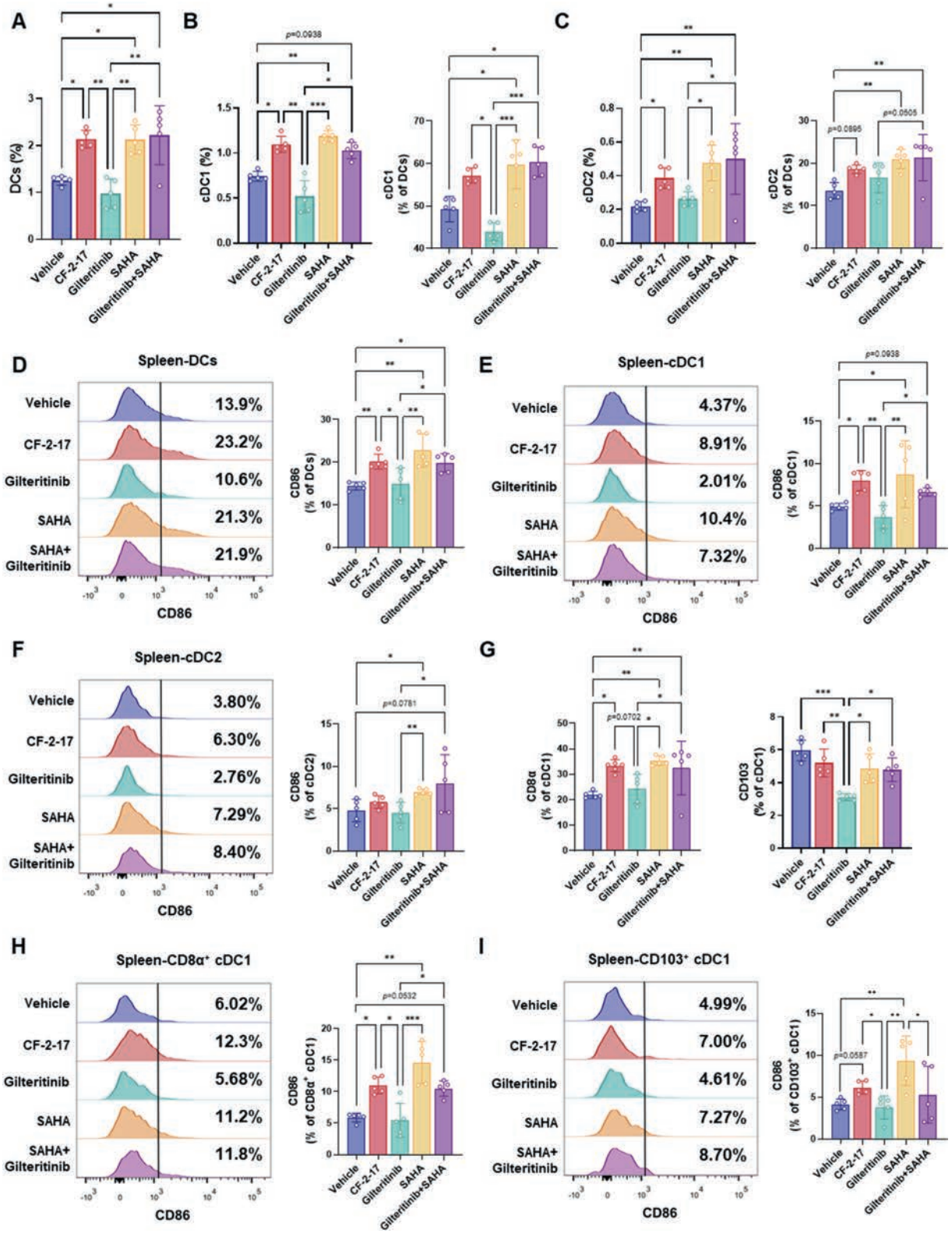

Figure 12 *In vivo* analysis of splenic dendritic cell subsets and activation. (A–C) The proportions of DCs (A), cDC1 (B), and cDC2 (C) in spleen of each group. (D–F) The expression of CD86 on DCs (D), cDC1 (E), and cDC2 (F) in spleen of each group. (G) The proportions of CD8α^+ cDC1 and CD103$^+$ cDC1 in spleen of each group. (H, I) The expression of CD86 on CD8α^+ cDC1 (H) and CD103$^+$ cDC1 (I) in spleen of each group. Data are expressed as mean ± SD from five biologically independent mice ($n = 5$). Statistical analysis was carried out between the data of each group (*$P < 0.05$, **$P < 0.01$ and ***$P < 0.001$).

$CD103^+$ cDC1 populations without affecting $CD8\alpha^+$ cDC1 (Fig. 12G—I), suggesting potential impairment of peripheral immune surveillance. Therefore, CF-2-17 enhances DC-mediated immunity by promoting DC accumulation and activation, contrasting with Gilteritinib's neutral or suppressive effects.

In addition, we isolated and induced mouse bone marrow-derived DCs (BMDCs), and validated the effects of the above compounds on DCs *in vitro*. The results showed that CF-2-17 could upregulate the expression of MHCII and CD86 in BMDCs and promote their antigen-presenting function, a phenomenon similar to that of SAHA (Fig. 13). Whereas Gilteritinib did not have this effect, similar to our *in vivo* results.

We further investigated whether CF-2-17 influences dendritic cell (DC) maturation *via* the NF-κB signaling pathway. The experimental results revealed that CF-2-17 treatment promoted the nuclear translocation of p65 (Fig. 14 A—C). Moreover, after p65 knockdown, the enhancing effect of CF-2-17 on the expression of CD86 and MHCII on DCs was significantly suppressed (Fig. 14 D—F). These findings suggest that CF-2-17 likely affects DC maturation by modulating the NF-κB signaling pathway, which is consistent with previous literature reports on the role of the NF-κB pathway in regulating DC maturation and function.

3. Conclusions

In the study, we performed structural optimization based on the previously identified FLT3/HDAC dual inhibitor **25h** and obtained new FLT3/HDAC dual inhibitor CF-2-17 with enhanced physicochemical properties while retaining nanomolar dual inhibition (FLT3 IC_{50} = 1.1 nmol/L; HDAC1 IC_{50} = 9.6 nmol/L). The introduction of hydrophilic groups conferred >150-fold higher aqueous solubility and improved HDAC1/HDAC6 selectivity *versus* **25h**. These improvements translated to superior pharmacokinetics and maintained oral bioavailability.

The development of FLT3/HDAC dual-target inhibitors represents a growing and promising therapeutic strategy[35,36]. Within this evolving field, CF-2-17 is distinguished by a distinct chemical scaffold and, more importantly, by a deepened biological investigation that expands its therapeutic scope. It not only demonstrated potent single-agent efficacy in FLT3-ITD-driven models, comparable to combination therapy with reduced toxicity, but also exhibited broad-spectrum activity against non-ITD hematologic malignancies and solid tumors, overcoming the limitation of single-target agents. Crucially, this study elucidates a previously underexplored immunomodulatory dimension: CF-2-17

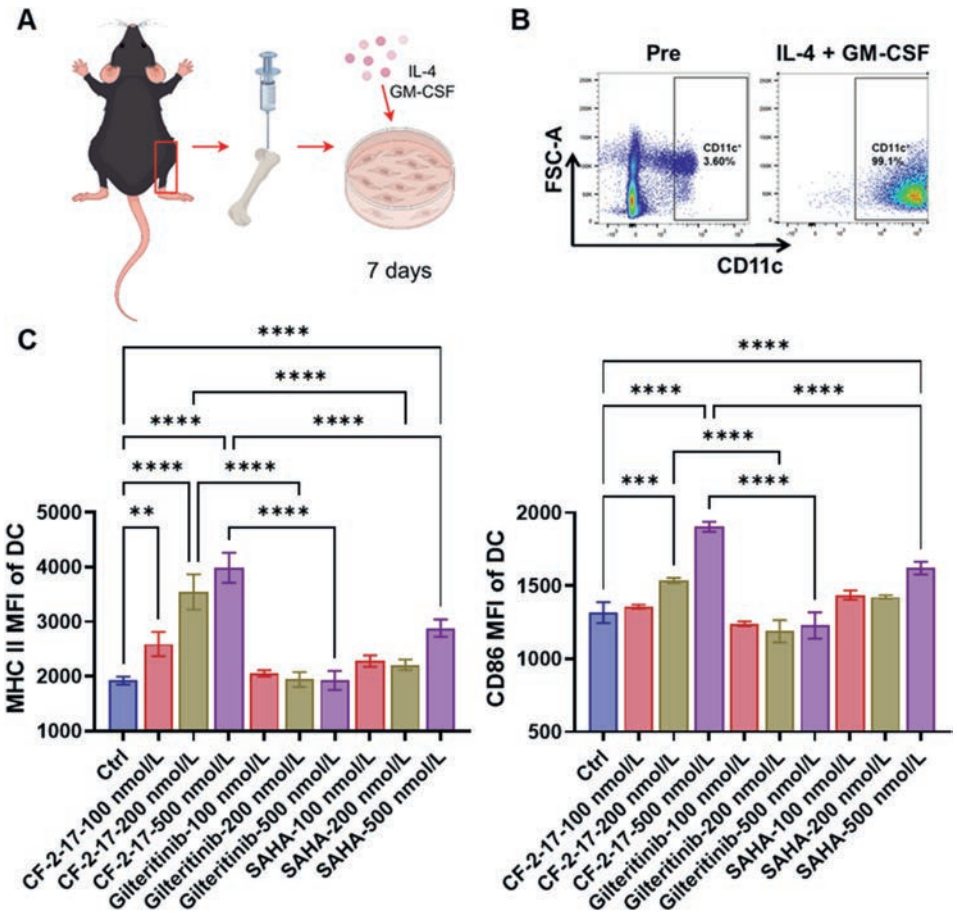

Figure 13 *In vitro* evaluation of CF-2-17 on dendritic cell maturation. (A) Schematic diagram of the isolation and induction of BMDCs. (B) Representative flow cytometry plots showing the purity of BMDCs. (C) Flow cytometry was performed to analyze the expressions of MHCII and CD86 on BMDCs treated with CF-2-17, Gilteritinib and SAHA. Data are expressed as mean ± SD from three independent biological replicates (n = 3). Statistical analysis was carried out between the data of each group (ns meaning no significant difference, $^{**}P < 0.01$, $^{***}P < 0.001$ and $^{****}P < 0.0001$).

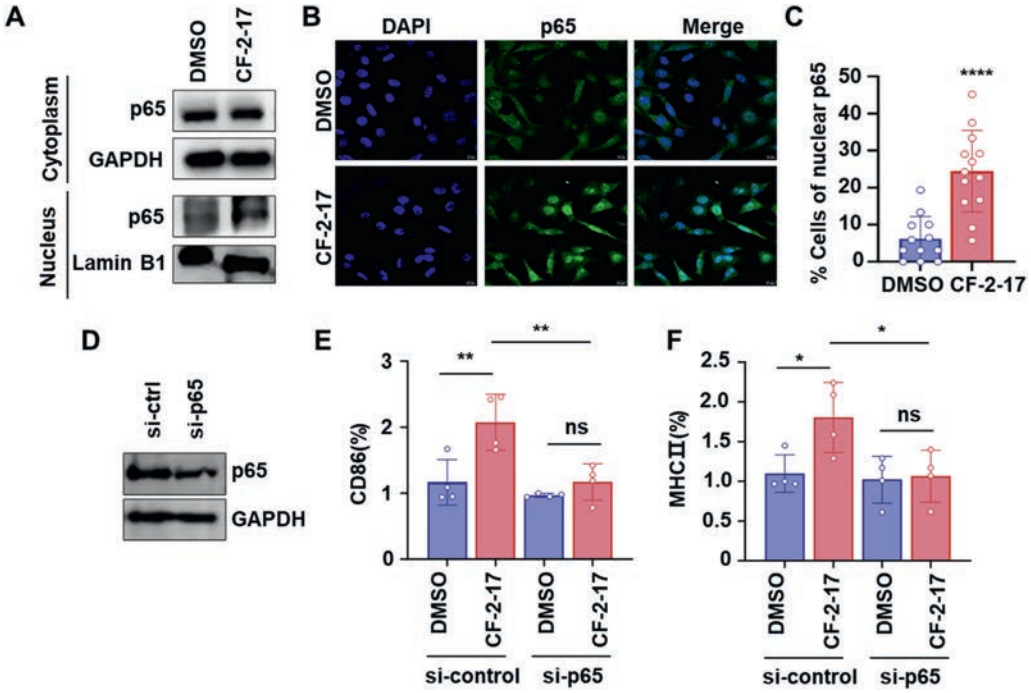

Figure 14 CF-2-17 promotes dendritic cell maturation *via* activation of the NF-κB pathway. (A) Western blot analysis shows total p65 protein levels in DC2.4 treated with or without CF-2-17 (100 nmol/L, 48 h). (B, C) Representative immunofluorescence images (B) and quantification (C) demonstrate CF-2-17-induced nuclear translocation of p65. (D) Validation of p65 knockdown efficiency in DC2.4 using siRNA. (E, F) Flow cytometric analysis confirms that p65 knockdown abrogates the CF-2-17-induced upregulation of CD86 (E) and MHCII (F) on DC2.4. Data are expressed as mean ± SD from four independent biological replicates ($n = 4$). Statistical analysis was carried out between the data of each group (ns meaning no significant difference, $^{*}P < 0.05$, $^{**}P < 0.01$ and $^{****}P < 0.0001$).

reprograms the tumor immune microenvironment by activating $CD8^{+}/CD4^{+}$ T cells and, uniquely, by rescuing FLT3 inhibitor-induced dendritic cell dysfunction *via* NF-κB pathway activation. Coupled with its rationally optimized pharmacokinetic profile, CF-2-17 exemplifies an advanced dual-inhibitor that integrates improved drug-like properties with novel immuno-epigenetic mechanisms.

Collectively, this work establishes CF-2-17 as a novel FLT3/HDAC dual inhibitor with enhanced pharmacokinetics and distinct immunotherapeutic potential, offering a promising strategy for the treatment of heterogeneous malignancies through coordinated epigenetic modulation and immune activation.

4. Experimental

4.1. General information

All reactions were monitored by thin-layer chromatography (TLC) was used to monitor reaction progression. Reagents and deuterium solvents (DMSO-d_6 or $CDCl_3$-d) were purchased from TCI, Bidepharm, Aladdin, Macklin and other solvents were supplied by Tianjin Fuyu Fine Chemical Com. Ltd. ^{1}H NMR (400 MHz), ^{13}C NMR (101 MHz) and High-resolution (ESI) mass spectra were conducted to verify the structures, which were obtained by Bruker DRX-400 and Impact II UHR-TOF mass spectrometers. The purity of all target compounds was determined by HPLC with a Shimadzu LC-20AT system and C_{18}-silica column (Thermo, 4.6 mm × 250 mm, 4 μm). The purity of all compounds is superior to 95%. Elution was done with methanol/water (85:15), and the flow rate was 0.6 mL/min. Mice were purchased from Charles River, and all procedures were approved by the Animal Ethics Committee of Shandong University.

4.2. Synthetic procedures

Please refer to Supporting Information for details.

4.3. Biology evaluation

4.3.1. HDAC inhibition assay

A testing system containing specific compound (50 μL), HDAC1, 2, 6, or 8 enzyme (10 μL), fluorescent substrate (40 μL, Ac-Leu-Gly-Lys (Ac)-AMC for HDAC1, 2, 6 or Boc-Lys (TFA)-AMC for HDAC8) was seeded into a 96-well black plate, followed by 1-h incubation at 37 °C. Then, the developer inclusive of trypsin (10 mg/mL) and panobinostat (2 μmol/L) was added and incubated for 20 min at 37 °C, after which a microplate reader was used for detecting fluorescence intensity (λex = 390 nm, λem = 460 nm). Finally, the fluorescence intensity was transformed to inhibitory activity using GraphPad Prism software.

4.3.2. Kinase inhibition assay

The assay was performed as described previously[37]. A reaction mixture containing the test compound, specific kinase (*e.g.*, 50 ng of FLT3), and its corresponding substrate (*e.g.*, 0.2 mg/mL MBP) in 50 μL of assay buffer (40 mmol/L Tris pH 7.4, 10 mmol/L $MgCl_2$, 0.1 mg/mL BSA, 1 mmol/L DTT, 10 μmol/L ATP) was incubated at 30 °C for 40 min in a 96-well plate. The test compounds were diluted in 10% DMSO, with 5 μL added per well (final DMSO concentration 1%). Following the reaction, kinase

activity was assessed using the Kinase-Glo® Plus Luminescence Assay kit, which quantifies remaining ATP (luminescent signal inversely correlates with kinase inhibition). Fluorescence intensity was measured, and dose-response curves along with IC_{50} values were generated *via* nonlinear regression analysis using GraphPad Prism software.

4.3.3. *In vitro anti-proliferative assay*

All cell lines were placed in the incubator filled with 5% CO_2 at 37 °C. MOLM-13, PC-9, and 293T cells were cultured in RPMI-1640 medium containing 10% fetal bovine serum (FBS) and 1% penicillin-streptomycin (P/S). MDA-MB-231 cells were cultured in DMEM medium containing 10% FBS and 1% P/S. The Ba/F3-FLT3-ITD and Ba/F3-FLT3-ITD-F691L cells were cultured in RPMI-1640 medium supplemented with 10% FBS and 1% P/S. A testing system containing cell suspension of 100 μL (1×10^4) and compound dilution of 100 μL was seeded into a 96-well plate and incubated for 48 h (Ba/F3-derived cells were incubated for 72 h), after which CCK-8 solution of 20 μL were added to terminate the incubation. The absorbance was recorded with a microplate reader ($\lambda = 450$ nm) and the values were used to calculate inhibitory rate or activity by GraphPad Prism software.

4.3.4. *Western blotting*

MOLM-13 cells (2×10^6 cells per well) were incubated with specific compounds, after which cells were harvested by centrifugation. Then, protein solutions were obtained by centrifugation after cell lysis. Next, loading buffer was added prior to protein degeneration at high temperature. Protein samples electrophoresed in 10% gels, followed by transferring to PVDF membranes. The membranes blocked with 5% defatted milk, washed with TBS buffer, incubated with primary antibodies, washed with TBS buffer, and incubated with secondary antibodies. After developing with ECL chemiluminescence solution, the signals were detected with Amersham Imager 600. The antibodies mentioned above were displayed as follows: Ac-H3 (CST, Cat #9649), H3K4me3 (UpingBio technology Co., Ltd., YP-Ab-01120), H3 (Abways, CY6587), Ac-α-tubulin (CST, Cat #5335), FLT3 (Abcam, Cat #ab245116), *p*-FLT3 (CST, Cat #3464), ERK1/2 (Abcam, Cat #ab184699), *p*-ERK1/2 (CST, Cat #4370T), STAT5 (CST, Cat #94205), p-STAT5 (Abcam, Cat #ab32364), GAPDH (Beyotime, AF1186), and HRP-labeled goat antirabbit IgG (H + L) (Beyotime, A0208).

4.3.5. *Whole-cell RNA transcriptome sequencing and analysis*

RNA sequencing was performed to profile the transcriptomic changes induced by CF-2-17 in MOLM-13 cells. Cells were seeded in 6-well plates at a density of 2×10^6 cells per well. After 12 h, they were treated with 50 nmol/L CF-2-17 or an equivalent volume of DMSO (solvent control) for 24 h. Following treatment, total RNA was extracted using TRIzol Reagent. RNA samples from three independent biological replicates per group were submitted to Tsingke Biotechnology Co., Ltd. for library construction and sequencing.

4.3.6. *Apoptosis assay*

MOLM-13 cells (1×10^6/well) were treated with selected compounds for 24 h prior to collection. After rinsing with PBS once, cells were stained through successive addition of binding solution (200 μL), Annexin V-FITC staining solution (2.5 μL), and PI staining solution (5 μL, Beyotime, C1062S). After a 15-min incubation in darkness, the samples were were subjected to analysis using a flow cytometer.

4.3.7. *Cell cycle assay*

MOLM-13 cells (1×10^6/well) were incubated with selected compounds for 24 h prior to collection. Cells were washed with PBS once, and then, immersed in 70% ethanol at 4 °C overnight. After removal of ethanol by centrifugation, cells were rinsed with PBS, subsequently, placed into RNase A solution (100 μL) for a 30-min incubation at 37 °C. Next, to the mixture was added PI staining solution (400 μL, Solarbio, CA1510) and incubated for 30 min at 4 °C. The samples were detected with a flow cytometry.

4.3.8. *Computational studies*

Protein receptor was obtained from RSCB PDB database and molecular docking was conducted with Glide[38]. After receiving energy minimization, ligands were proceeded to conformational search, obtaining conformational databases. Then, all conformations were docked into the protein receptor. The pose ranked first was retain and UCSF Chimera software was adopted to visualize the docking result[39].

Based on the docking results, unbiased MD simulations were performed using the Desmond module in the Schrödinger suite for CF-2-17 complexed with HDAC1 and HDAC6. The system was solvated in a 10 Å SPC water box, neutralized, and supplemented with 0.15 mol/L NaCl. Following equilibration, a 100 ns NPT molecular dynamics simulation was carried out at 300 K and 1 atm.

4.3.9. *Mitochondrial depolarization assay*

After treatment with selected compounds, MOLM-13 cells (5×10^5/well) were collected and washed with PBS once. Then, cells were immersed in TMRE working solution (0.5 mL, Beyotime, C2001S) for 30 min at 37 °C. Subsequently, working solution and cells was separated by centrifugation. Finally, cells were transferred to a black 96-well plate prior to detection of fluorescence intensity (λex = 540 nm, λem = 579 nm).

4.3.10. *Stability of mouse liver microsomes*

Firstly, the samples were prepared and inclusive of compounds (20 μL, 2 mg/mL in methanol), mouse liver microsomes (100 μL, 4 mg/mL in PBS), NADPH (100 μL, 4 mmol/L in PBS), and $MgCl_2$ (180 μL, 6 mmol/L in PBS), and co-incubated for 0, 10, 20, 30, 60, 90, and 120 min at 37 °C. Subsequently, these samples were terminated by addition of ice acetonitrile (400 μL) for 15 min at 4 °C. Finally, the supernatant obtained by sample centrifugation was analyzed by HPLC (Shimadzu LC-20AT).

The natural logarithm of the percent drug remaining at each time point was plotted against the incubation time. The first-order elimination rate constant k (min^{-1}) was derived from the slope of the linear regression analysis. The *in vitro* half-life and intrinsic clearance were then calculated using Eqs. (1) and (2):

$$t_{1/2}(\text{min}) = -\frac{0.693}{k} \quad (1)$$

$$\mathrm{CL}_{\mathrm{int,\ \textit{in vitro}}}\ (\mathrm{mL}\,/\,\mathrm{min}\,/\,\mathrm{mg\ protein}) = \left(\frac{0.693}{t_{1/2}}\right) \times \frac{\text{Incubation volume (mL)}}{\text{Microsomal protein mass (mg)}} \quad (2)$$

4.3.11. Stability of mouse plasma

Mouse plasma (250 μL) was incubated with compound solution (125 μL, 2 mg/mL in methanol) for 0, 0.5, 1, 3, 6, 9, 12, and 24 h at 37 °C. After addition of ice acetonitrile (600 μL), the supernatant was obtained by centrifugation prior to HPLC analysis (Shimadzu LC-20AT).

4.3.12. Water solubility assay

Firstly, selected compounds were dissolved in methanol to prepare stock solutions (2 mg/mL), which were diluted to obtain a series of clarified solution with gradient concentration, including 1000, 500, 250, 62.5, 15.625, 3.9063, 0.977, 0.244 μg/mL. Subsequently, these samples were analyzed through HPLC (Shimadzu LC-20AT), thus establish the connection between concentration and peak area, specifically the concentration−peak area standard curve. Then, the supersaturated solutions of selected compounds were prepared with deionized water and phosphate buffers (pH = 2.0 and 7.0) in EP tubes. After ultrasonic concussion for 1 h, these samples were placed in a shaker (800 rpm) at room temperature for 24 h. Next, these samples were centrifuge to obtain liquid supernatant at 12,000 rpm prior to HPLC analysis. Finally, the water solubility was calculated using the standard curves.

4.3.13. Pharmacokinetics study

All animal experiments accorded with the protocol approved by the Laboratory Animal Center of Shandong University. The experimental SD rats were fed adaptively for one week. Then, rats were dosed with selected compound at 1 mg/kg (i.v.) after being fasted for 12 h. Blood samples were collected by heparin sodium anticoagulation tubes from the cheek at 5, 15, 30 min, 1, 2, 4, 6, 8 and 24 h, followed by storing at 0 °C for more than 15 min. The plasma was separated by centrifuging the samples for 3 min at 6000 rpm, and stored at −20 °C. Finally, the plasma concentration of each indicated time was determined by LC−MS/MS, and PK parameters were calculated by WinNolin8.2 software.

4.3.14. MOLM-13 xenograft tumor model

Cultured MOLM-13 cells were washed twice with PBS. A suspension containing 5×10^6 cells in a mixture of 70 μL PBS and 30 μL Matrigel (ABWBIO, #0827245) was subcutaneously inoculated into the right axilla of six-week-old BALB/c nude mice. When tumor volumes reached a predetermined size, mice were randomized into groups and treated *via* oral gavage once daily for 9 consecutive days. Treatment groups included: vehicle control, 30 mg/kg SAHA, 10 mg/kg Gilteritinib, and 10 mg/kg CF-2-17. Tumor volume and mouse body weight were measured every other day.

4.3.15. K562 xenograft tumor model

Harvested K562 cells were washed twice with PBS. A suspension of 5×10^6 cells in an identical PBS/Matrigel matrix was subcutaneously injected into the right flank of six-week-old BALB/c nude mice. Five days post-inoculation (designated Day 0), when tumor volumes approached the threshold, mice were randomized into six groups for treatment *via* oral gavage once daily for 16 consecutive days. Groups comprised: vehicle control, 20 mg/kg CF-2-17, 10 mg/kg Gilteritinib, 30 mg/kg SAHA, 20 mg/kg **25h**, and 50 mg/kg CUDC-907. Tumor volume and body weight were measured every 3 days using Vernier calipers. On Day 16, all mice were euthanized, tumors were excised, photographed, and weighed.

4.3.16. LLC homograft tumor model

Mice were housed under specific pathogen-free (SPF) conditions at the Model Animal Research Centre of Shandong University with *ad libitum* access to food and water. To establish the LLC syngeneic tumor model, LLC cells in the logarithmic growth phase were harvested and resuspended in sterile PBS at a density of 5×10^6 cells/100 μL. Each mouse was subcutaneously inoculated with 100 μL of cell suspension in the left flank. On Day 6 post-inoculation, when palpable tumors had formed, mice were randomly assigned to treatment groups (n = 5/group) and administered 30 mg/kg SAHA, 10 mg/kg Gilteritinib, or 10/20 mg/kg CF-2-17 *via* oral gavage once daily for 15 days. Tumor length (L) and width (W) were measured and tumor volume was calculated using Eq. (3):

$$\text{Volume } (\mathrm{mm}^3) = 0.5 \times L \times W^2 \quad (3)$$

All experiments complied with AAALAC International guidelines for humane animal care.

4.3.17. Isolation of lymphocytes from tumors and spleen

For the tumor tissues, the mice were euthanized and the subcutaneous tumor tissues were isolated and washed with 1 × PBS. Then add 5 mL of tumor digesting solution (5 mL DMEM containing 0.1 mL FBS, 50 mg collagenase IV and 2.5 μL hyaluronidase). The tissues were minced, transferred to 15 mL centrifuge tubes, and digested for 30 min at 37 °C, with 2−3 times of inverted mixing during the period. The digested tissues were ground through a 200-mesh sieve into a new centrifuge tube and centrifuged at 100×g for 1 min. Transfer the supernatant into a new tube and centrifuge at 400×g for 5 min. Discard the supernatant and resuspend the cells with 5 mL 40% Percoll followed by centrifuging at 800×g for 25 min. The supernatant was discarded carefully and the inside of the tubes were wiped. Then add 4 mL red blood cell (RBC) lysis solution to resuspend cells and incubate for 15 min at 4 °C. Add 1 × PBS to terminate RBC lysis and centrifuge at 400×g for 5 min to collect the cells. Resuspend cells with 1 × PBS and filter through a strainer.

The splenic lymphocytes, spleen tissues were isolated, minced and ground directly through a 200-mesh sieve. Centrifuge at 400×g for 5 min, add 4 mL RBC lysis solution to resuspend cells and incubate for 15 min at 4 °C. Then centrifuge at 400×g for 5 min again and discard the supernatant. Resuspend cells with 1 × PBS and filter through a strainer.

4.3.18. Flow cytometry

For cell surface molecule detection, rat serum was added in the cell suspension to block the cells at room temperature for 30 min. Subsequently, stained with fluorescein-conjugated antibodies at 4 °C for 1 h. 1 × PBS was added to wash away unbound antibodies.

For intracellular cytokine detection, cells were first resuspended in 1640 medium, seeded into 24-well plates and pretreated with ionomycin (1 μg/mL), PMA (50 ng/mL), and Brefeldin A

(1 μL/mL). After 4 h, cells were harvested and washed with 1 × PBS. After blocking with rat serum and stained with antibodies targeting surface molecule, cells were fixed with 150 μL 4% paraformaldehyde at 4 °C for 30 min. After washing with 1 × PBS, 150 μL of permeabilization wash buffer containing 10% rat serum was added for permeabilization at room temperature for 30 min. After washed with 1 × PBS, corresponding fluorescein-conjugated antibodies for intracellular cytokines were added and incubate at 4 °C for 1 h. Add 1 × PBS to wash away unbound antibodies. Data were collected using BD FACSymphony A3 (BD Biosciences), and analyzed with FlowJo software (FlowJo, LLC, Ashland, OR, USA). The antibodies used in the experiment were listed in Supporting Information Table S3.

4.3.19. In vitro induction of BMDCs

C57BL/6J mice were euthanized aseptically, and femurs and tibiae were harvested. Cut the ends of the femur and tibia, and flush the bone marrow cavity several times with 1 × PBS using syringe to collect cell suspension in bone marrow. Centrifuge cell suspension at 400×*g* for 5 min and then discard the supernatant. The cell pellet was resuspended in 3−5 mL red blood cell (RBC) lysis buffer and incubated at 4 °C for 10 min. RBC lysis was terminated with 1 × PBS, followed by centrifugation at 400×*g* for 5 min. The pellet was resuspended in complete RPMI-1640 medium supplemented with recombinant mouse IL-4 (rmIL-4; 5 ng/mL) and recombinant mouse GM-CSF (rmGM-CSF; 10 ng/mL). Seed the cells into 6-well plate and incubated at 37 °C with 5% CO_2. After 48 h, the medium containing non-adherent cells was discarded and fresh medium containing cytokines was added. On Day 5, half of the medium was replaced with fresh medium and cultured to Day 7. Finally, all cells were collected gently to obtain BMDCs.

4.3.20. Acute toxicity study in mice

The acute toxicity of CF-2-17 was assessed in C57BL/6J mice. Mice were randomly divided into three groups ($n = 5$): vehicle control, low-dose (10 mg/kg), and high-dose (50 mg/kg) CF-2-17. Following an overnight fast, a single dose was administered *via* intragastric gavage.

To evaluate potential hematological toxicity, blood was collected from the submandibular venous plexus at 48 h post-dosing. A comprehensive panel of hematological parameters, including complete blood count and differential leukocyte counts, was analyzed using an automated hematology analyzer.

To assess hepatotoxicity, serum was collected on Day 5 post-administration. Alanine aminotransferase (ALT) and aspartate aminotransferase (AST) levels were quantified using commercial assay kits (Nanjing Jiancheng Bioengineering Institute). General systemic toxicity was monitored by recording body weight daily for 7 consecutive days.

4.3.21. Immunohistochemical staining

Immunohistochemical (IHC) staining for PD-L1 was performed on paraffin-embedded tumor tissue sections. After deparaffinization and rehydration, endogenous peroxidase activity was blocked with 3% H_2O_2. Antigen retrieval was performed using citrate-EDTA buffer (Beyotime, #P0086) with heat treatment.

Sections were blocked with goat serum and then incubated overnight at 4 °C with a primary antibody against PD-L1 (Abmart, #M033179). Following PBS washes, detection was carried out using a streptavidin-biotin detection system (Zhongshan Golden Bridge, SP-9000) with DAB (Gene Tech, GK600505) as the chromogen. Sections were counterstained with hematoxylin, dehydrated, cleared, and mounted with neutral resin. Stained slides were examined and imaged using an inverted fluorescence microscope.

4.3.22. H&E staining

The mice of posttreatment were euthanized, followed by dissection to obtain tumor tissues and different organs, which were immersed in 4% paraformaldehyde solution and further processed into paraffin samples. Then, these paraffin samples underwent cutting to obtain paraffin sections. After deparaffination and hydration, the sections were stained with hematoxylin and eosin (H&E). Finally, the samples were imaged with a microscope after dehydration with alcohol of gradient concentration (80%−100%).

4.3.23. siRNA transfection

For p65 knockdown, DC2.4 cells were seeded in 6-well plates and allowed to adhere for 24 h. Transfection was performed using Jet Polyplus Transfection reagent with a synthetic siRNA oligonucleotide targeting p65 (sense strand: 5′-UCAGCACCAUCAACUUUGAtt-3′, Sangon Biotech). A non-targeting siRNA was used as a negative control. Following a 48-h transfection period, knockdown efficiency was confirmed by Western blot analysis. The transfected cells were then treated with or without 100 nmol/L CF-2-17 for an additional 48 h, harvested, and subjected to flow cytometric analysis of surface markers after staining with fluorochrome-conjugated antibodies. Data were acquired on a FACS Celesta flow cytometer (BD Biosciences).

4.3.24. Nuclear and cytoplasmic protein extraction

To assess p65 subcellular localization, DC2.4 cells were cultured in 10-cm dishes and treated with 100 nmol/L CF-2-17 for 48 h. Nuclear and cytoplasmic proteins were subsequently fractionated using a commercial extraction kit (Nuclear and Cytoplasmic Protein Extraction Kit, Beyotime, #P0027) strictly according to the manufacturer's protocol. The protein expression levels of p65 in each fraction were then analyzed by Western blot.

4.3.25. Statistical analysis

All experimental data derived from results of three or more independent assays. Two-tailed Student's *t*-test was conducted to evaluate whether there were significant differences between sample data. *P* value below 0.05 indicates there exist significant differences between two set of selected data.

Acknowledgments

We genuinely thank the Advanced Medical Research Institute, Shandong University, for their help in the experiments. This work was supported by the Noncommunicable Chronic Diseases-National Science and Technology Major Project (2023ZD0507700 and 2023ZD0507704) the National Natural Science Foundation of China (22477070 and 22377068), the Taishan Scholar Programme of Shandong Province (tstp.20230606), the Key R&D Program of Shandong Province (2025CXPT121) and the Shandong Provincial Youth Innovation Team Development Program (2023KJ026).

Author contributions

Xuben Hou, Hao Fang, and Wei Zhao initiated the project and supervised the research. Yingjie Chang performed the drug design and synthesis. Yingjie Chang, Xue Li, Huirui Wang, and Huajun

Zhao carried out the experiments and processed the data. Yue Zhou, Wenchao Bi, Ruixue Cheng, Yuxin Shi, He Weng, and Xinying Yang participated in part of the experiments and validated the data. Hao Fang, Wei Zhao, Xuben Hou, Yingjie Chang, and Xue Li discussed and analyzed the data. Xuben Hou, Yingjie Chang, and Xue Li wrote and revised the manuscript. All authors have read and approved the final manuscript.

Conflicts of interest

The authors declare no conflicts of interest.

Appendix A. Supporting information

Supporting information to this article can be found online at https://doi.org/10.1016/j.apsb.2026.05.025.

References

1. Ocio EM, Herrera P, Olave MT, Castro N, Perez-Simon JA, Brunet S, et al. Panobinostat as part of induction and maintenance for elderly patients with newly diagnosed acute myeloid leukemia: phase Ib/II panobidara study. *Haematologica* 2015;**100**:1294−300.
2. Massaro C, Sgueglia G, Muro A, Pieragostino D, Lanuti P, Cufaro MC, et al. Vorinostat impairs the cancer-driving potential of leukemia-secreted extracellular vesicles. *J Transl Med* 2025;**23**: 421.
3. Gu SY, Hou Y, Dovat K, Dovat S, Song CH, Ge Z. Synergistic effect of HDAC inhibitor chidamide with cladribine on cell cycle arrest and apoptosis by targeting HDAC2/c-Myc/RCC1 axis in acute myeloid leukemia. *Exp Hematol Oncol* 2023;**12**:23.
4. Bachy E, Camus V, Thieblemont C, Sibon D, René-Olivier C, Ysebaert L, et al. Romidepsin plus CHOP *versus* CHOP in patients with previously untreated peripheral T-cell lymphoma: results of the Ro-CHOP phase III study (conducted by LYSA). *J Clin Oncol* 2022; **40**:242−51.
5. Liang T, Wang FL, Elhassan RM, Cheng YM, Tang XL, Chen WG, et al. Targeting histone deacetylases for cancer therapy: trends and challenges. *Acta Pharm Sin B* 2023;**13**:2425−63.
6. Ho TCS, Chan AHY, Ganesan A. Thirty years of HDAC inhibitors: 2020 insight and hindsight. *J Med Chem* 2020;**63**:12460−84.
7. Rai S, Kim WS, Ando K, Choi I, Izutsu K, Tsukamoto N, et al. Oral HDAC inhibitor tucidinostat in patients with relapsed or refractory peripheral T-cell lymphoma: phase IIb results. *Haematologica* 2022; **108**:811−21.
8. Lechner S, Malgapo MIP, Grätz C, Steimbach RR, Baron A, Rüther P, et al. Target deconvolution of HDAC pharmacopoeia reveals MBLAC2 as common off-target. *Nat Chem Biol* 2022;**18**:812−20.
9. Havas AP, Tula-Sanchez AA, Steenhoek HM, Bhakta A, Wingfield T, Huntley MJ, et al. Defining cellular responses to HDAC-selective inhibitors reveals that efficient targeting of HDAC3 is required to elicit cytotoxicity and overcome naïve resistance to pan-HDACi in diffuse large B cell lymphoma. *Transl Oncol* 2024;**39**:101779.
10. Sun LM, Liu YF, Guo XY, Cui TM, Wu CH, Tao J, et al. Acetylation-dependent regulation of core spliceosome modulates hepatocellular carcinoma cassette exons and sensitivity to PARP inhibitors. *Nat Commun* 2024;**15**:5209.
11. Chang TY, Yan Y, Yu ZY, Rathore M, Lee NZ, Tseng HJ, et al. Combined HDAC8 and checkpoint kinase inhibition induces tumor-selective synthetic lethality in preclinical models. *J Clin Investig* 2024;**134**:e165448.
12. Zhou Y, Liu XT, Xue JX, Liu LL, Liang T, Li W, et al. Discovery of peptide boronate derivatives as histone deacetylase and proteasome dual inhibitors for overcoming Bortezomib resistance of multiple myeloma. *J Med Chem* 2020;**63**:4701−15.
13. Liang T, Zhou Y, Elhassan RM, Hou XB, Yang XY, Fang H. HDAC−Bax multiple ligands enhance Bax-dependent apoptosis in HeLa cells. *J Med Chem* 2020;**63**:12083−99.
14. Liu M, Gao S, Liang T, Qiu XT, Yang XY, Fang H, et al. Discovery of novel Src Homology-2 domain-containing phosphatase 2 and histone deacetylase dual inhibitors with potent antitumor efficacy and enhanced antitumor immunity. *J Med Chem* 2022;**65**:12200−18.
15. Chen C, Li X, Zhao HJ, Liu M, Du JT, Zhang J, et al. Discovery of DNA-targeting HDAC inhibitors with potent antitumor efficacy *in vivo* that trigger antitumor immunity. *J Med Chem* 2022;**65**:3667−83.
16. Chang YJ, Guo HH, Li X, Zong LY, Wei JL, Li ZH, et al. Development of a first-in-class DNMT1/HDAC inhibitor with improved therapeutic potential and potentiated antitumor Immunity. *J Med Chem* 2024;**67**:16480−504.
17. Yao MY, Yan WZ, Wang YF, Zhao Y, Xu XW, Chen YJ, et al. IHCH9033, a novel class I HDAC inhibitor, synergizes with FLT3 inhibitor and rescues quizartinib resistance in FLT3-ITD AML *via* enhancing DNA damage response. *Exp Hematol Oncol* 2025;**14**: 15.
18. Short NJ, Nguyen D, Ravandi F. Treatment of older adults with FLT3-mutated AML: emerging paradigms and the role of frontline FLT3 inhibitors. *Blood Cancer J* 2023;**13**:142.
19. Schlenk RF, Kayser S, Bullinger L, Kobbe G, Casper J, Ringhoffer M, et al. Differential impact of allelic ratio and insertion site in FLT3-ITD−positive AML with respect to allogeneic transplantation. *Blood* 2014;**124**:3441−9.
20. Schneider F, Hoster E, Schneider S, Dufour A, Benthaus T, Kakadia PM, et al. Age-dependent frequencies of NPM1 mutations and FLT3-ITD in patients with normal karyotype AML (NK-AML). *Ann Hematol* 2012;**91**:9−18.
21. Yamamoto Y, Kiyoi H, Nakano Y, Suzuki R, Kodera Y, Miyawaki S, et al. Activating mutation of D835 within the activation loop of FLT3 in human hematologic malignancies. *Blood* 2001;**97**:2434.
22. Grob T, Sanders M, Vonk C, Kavelaars FG, Rijken M, Hanekamp D, et al. Prognostic value of FLT3-internal tandem duplication residual disease in acute myeloid leukemia. *J Clin Oncol* 2022;**41**:756−65.
23. Dinardo CD, Tiong IS, Quaglieri A, Macraild S, Loghavi S, Brown FC, et al. Molecular patterns of response and treatment failure after frontline venetoclax combinations in older patients with AML. *Blood* 2020;**135**:791−803.
24. Smith CC, Wang Q, Chin CS, Salerno S, Damon LE, Levis MJ, et al. Validation of ITD mutations in FLT3 as a therapeutic target in human acute myeloid leukaemia. *Nature* 2012;**485**:260−3.
25. Chang YJ, Li X, Zhou Y, Yang XY, Zhao W, Fang H, et al. Simultaneous inhibition of FLT3 and HDAC by novel 6-ethylpyrazine-2-carboxamide derivatives provides therapeutic advantages in acute myelocytic leukemia. *Eur J Med Chem* 2024;**279**:116847.
26. Zhang ZX, Hu RX, Liu J, Yang XH, Xiao YB, Xu X, et al. Antitumor activity of gilteritinib, an inhibitor of AXL, in human solid tumors. *Cell Death Discov* 2025;**11**:124.
27. Miller KM, Tjeertes JV, Coates J, Legube G, Polo SE, Britton S, et al. Human HDAC1 and HDAC2 function in the DNA-damage response to promote DNA nonhomologous end-joining. *Nat Struct Mol Biol* 2010; **17**:1144−51.
28. Li YS, Yang CX, Xie LL, Shi F, Tang M, Luo XJ, et al. CYLD induces high oxidative stress and DNA damage through class I HDACs to promote radiosensitivity in nasopharyngeal carcinoma. *Cell Death Dis* 2024;**15**:95.
29. Xu YQ, Chen Y, Zhang JG, Wang JC, Yang S, Zhao HK, et al. RNASET2 deficiency induces hepatocellular carcinoma metastasis through cholesterol-triggered MET activation. *Adv Sci* 2025;**12**: e2411888.
30. Liu BW, Sun N, Lin H, Zhou XJ, Ma HY, Wang X, et al. The p53/ZEB1-PLD3 feedback loop regulates cell proliferation in breast cancer. *Cell Death Dis* 2023;**14**:751.
31. Keller AM, Schildknecht A, Xiao YL, van den Broek M, Borst J. Expression of costimulatory ligand CD70 on steady-state dendritic

cells breaks CD8 T cell tolerance and permits effective immunity. *Immunity* 2008;**29**:934−46.
32. Lu JJ, Peng YC, Huang RH, Feng ZJ, Fan YY, Wang HJ, et al. Elevated TYROBP expression predicts poor prognosis and high tumor immune infiltration in patients with low-grade glioma. *BMC Cancer* 2021;**21**:723.
33. Deng SY, Hu QW, Zhang H, Yang F, Peng C, Huang CX. HDAC3 inhibition upregulates PD-L1 expression in B-cell lymphomas and augments the efficacy of anti-PD-L1 therapy. *Mol Cancer Ther* 2019; **18**:900−8.
34. Zhou Y, Du JT, Li X, Zhao HJ, Xue JX, Liu YC, et al. Preclinical characterization of SDFZ-8, a highly potent HDAC1 inhibitor, for cancer immunotherapy. *MedComm* 2025;**6**:e70500.
35. Tian H, Liu YC, Lin SW, Deng JL, Zhang QH, Hao F, et al. Design, synthesis, and biological evaluation of novel Fms-like tyrosine kinase 3/VEGFR2/histone deacetylase inhibitors for the treatment of acute myeloid leukemia. *J Med Chem* 2025;**68**:5736−59.
36. Wang ZJ, Wu DL, Zhao XF, Liu CL, Jia SM, He QD, et al. Rational discovery of dual FLT3/HDAC inhibitors as a potential AML therapy. *Eur J Med Chem* 2023;**260**:115759.
37. Kashem MA, Nelson RM, Yingling JD, Pullen SS, Prokopowicz AS, Jones JW, et al. Three mechanistically distinct kinase assays compared: measurement of intrinsic ATPase activity identified the most comprehensive set of ITK inhibitors. *J Biomol Screen* 2007;**12**:70−83.
38. Friesner RA, Banks JL, Murphy RB, Halgren TA, Klicic JJ, Mainz DT, et al. Glide: a new approach for rapid, accurate docking and scoring 1 method and assessment of docking accuracy. *J Med Chem* 2004;**47**:1739−49.
39. Pettersen EF, Goddard TD, Huang CC, Couch GS, Greenblatt DM, Meng EC, et al. UCSF chimera−A visualization system for exploratory research and analysis. *J Comput Chem* 2004;**25**:1605−12.